EUROPEAN ORGANIZATION FOR NUCLEAR RESEARCH

CERN-PPE/93-21
January 13, 1993

Test Results of a Fully Projective Lead/Scintillating-Fiber Calorimeter

The RD1 Collaboration

J. Badier[1], N. Bouhemaid[2], S. Buontempo[3], P. Busson[1], L. Calôba[4], P. Cattaneo[5], C. Charlot[1], A. Chekhtman[6], M-C. Cousinou[6], S. Dagoret[7], A. Dell'Acqua[5], E. Duchovni[13], A. Ereditato[3], R. Ferrari[5], D. Fouchez[6], L. Fredj[2], G. Fumagalli[5], J-M. Gaillard[8,10], G. Goggi[5], A. Gomes[9], T. Hansl-Kozanecka[7], A. Henriques[8,9], P. Jenni[8], F. Kovacs[7], D. Lellouch[13], L. Levinson[13], L. Linssen[8], M. Livan[5], J. Lory[7], N. Lupu[13], A. Maio[9,11], B. Michel[2], G. Mikenberg[13], G. Montarou[2], R. Nacasch[6], E. Nagy[6], D. Pallin[2], E. Pennacchio[5], L. Peralta[9], L. Poggioli[8], G. Polesello[5], F. Riccardi[3], A. Rimoldi[5], J.M. Seixas[4,8], M.N. Souza[4], Z.D. Thomé[4], S. Tisserant[6], B. Tomé[9], F. Vazeille[2], V. Vercesi[5], R. Wigmans[12], R. Zitoun[7]

1) *LPNHE, Ecole Polytechnique, Palaiseau, France*
2) *LPPCF, Université Blaise Pascal, Clermont-Ferrand, France*
3) *Università di Napoli and INFN Sez. Napoli, Italy*
4) *COPPE/EE/UFRJ, Rio de Janeiro, Brazil*
5) *Università di Pavia and INFN Sez. Pavia, Italy*
6) *CPPM, Marseille, France*
7) *LPNHE, Université Paris VI&VII, Paris, France*
8) *CERN, Geneva, Switzerland*

9) *LIP, Lisbon, Portugal*

10) *LAL, Orsay, France*

11) *CFNUL, Lisbon, Portugal*

12) *Texas Tech University, Lubbock, USA*

13) *Weizmann Institute, Rehovot, Israel*

Abstract

We report on an experimental study of the properties of a modular lead/scintillating-fiber calorimeter with a fully projective tower geometry. Although the calorimeter structure is monolythic, an effective segmentation into an electromagnetic and an hadronic section is achieved by separating the readout of the fibers running throughout the calorimeter from those starting beyond a depth of ~ 25 radiation lengths. This feature is used for e/π separation. Discontinuities in the sampling fraction near the boundaries of the modules cause a signal nonuniformity for electrons, which can be corrected. Similar effects observed for high energy hadrons are discussed. Results are given on the energy and position resolution for electrons, on the signal linearity and on the absolute light yield. Pion showers were only partially contained in this detector. The information from a backing calorimeter, consisting of fast thin-gap wire chambers interleaved by iron slabs, significantly improves the energy resolution of the incompletely contained pion showers.

(Submitted to Nuclear Instruments and Methods in Physics Research)

1. INTRODUCTION

The use of scintillating fibers as active material in calorimeters has a number of attractive features in termes of speed, ease of read-out and hermiticity of the detector. Scintillating fibers deliver fast signals[1-3] at very low noise level[4,5], allow for a compact detector, can operate in Mrad/yr radiation environments[6,7] and can lead to a cheap detector design. In addition the calorimeter can be made compensating by an appropriate choice of the absorber and the sampling fraction[8,9]. Because of these reasons, scintillating-fiber calorimeters are considered an attractive option for experiments at the future multi-TeV proton-proton colliders LHC and SSC[10,11,12].

The basic calorimetric properties for electron, hadron, jet and muon detection of this type of calorimeter were extensively studied by Acosta et al.[2,9,13,14]. However, the authors used generic prototypes for these studies. The detectors were not modular, the tower structure was achieved by grouping the fibers coming out of the lead pile. Moreover, a cylindrical geometry was used. In a realistic application of this type of calorimeter in a $\simeq 4\pi$ collider experiment, the detector has to consist of projective modules, pointing (approximately) to the interaction vertex. In this paper, we report on the results of a first attempt to construct such a detector.

Although the projectivity requirement considerably complicates the construction and the calibration of the calorimeter, there are major bonuses in terms of performance, as will be shown. Firstly, the tower size is much better adapted to the natural shower dimensions of the particles to be detected. Secondly, an effective segmentation into an electromagnetic (e.m.) and an hadronic section can be achieved in an elegant way. Since the fibers are running in the same direction as the particles, explicit longitudinal segmentation is a largely nontrivial problem for this type of detectors.

The fiber calorimeter was tested in conjunction with an iron backing calorimeter read out with fast thin-gap wire chambers. This detector proved to be quite useful to study events with showers starting deep inside the fiber calorimeter. Moreover, it provided remarkably detailed and important information concerning the nature of the escaping shower particles.

In section 2, the detectors, their construction and calibration and the experimental setup are described. Details of the analysis of the experimental data are given in section 3. The experimental results are presented in section 4. Section 5 contains a summary and the conclusions.

2. EXPERIMENTAL SETUP

2.1 The detectors

The measurements were performed with a calorimeter consisting of monolythic projective modules. The modules had the shape of one quadrant of a truncated pyramid, with a front face of about 4×4 cm^2, a back face of about 10×10 cm^2 and a length (depth) of 200 cm. Therefore, these modules can be considered as elements of a projective calorimeter with an inner radius of 130 cm, each covering an area $\Delta\eta \times \Delta\phi \approx 0.03 \times 0.03$.

Each module contains 2346 scintillating plastic fibers with a diameter of 1.0 mm* . These fibers form the active part of the sampling calorimeter. They are embedded in a lead matrix in such a way that each fiber is equidistant from its 6 neighbors (fig. 1a). The fiber spacing is 2.22 mm (center to center), which gives a volume ratio lead to fiber of about 4:1, chosen as such to make the calorimeter (approximately) compensating[9] . All fibers run parallel to one another in the direction of the incoming particles. Therefore, some of them run all the way from the front face to the back, whereas the fibers in the sloping part of the module become increasingly shorter as they approach the outer edge. These fibers start at progressively increasing distances from the front face of the module, with a pitch of about 7 cm (fig. 1b).

We took advantage of this feature to obtain some kind of "longitudinal" segmentation in the readout. All fibers running up to the front face of the calorimeter and the first two rows of shorter fibers were bunched together and named "electromagnetic section". The remaining fibers, which start at 20 cm from the front face and beyond, were also bunched together and named "hadronic section" (fig. 1b). The e.m. section of each module contains 399 fibers, the hadronic section 1947.

The modules were constructed in the following way. First the lead structure was assembled. Its basic components are extruded grooved lead plates of the desired length, with half holes on each side. A 5 μm thick layer of tin was deposited electrolytically on each side of these plates. Next, the plates were stacked in parallepiped blocks with a cross section of about 10×14 cm^2 and brazed together by heating the stack for 12-14 hours at a temperature of 245°C. The resulting blocks were then machined in such a way that two modules with the desired geometry were obtained from each block. The fibers were then inserted in the holes, from the rear end. Obviously, the tolerances, both on the diameter of the fibers and of the holes, are extremely important. The extruded plates were made in such a way that the resulting holes had a nominal diameter of 1.1 mm, which leaves a free space of 50 μm on each side of the fiber. After some cleaning of holes that were partially obstructed by tin residuals, we managed to get typically 98% of the fibers in place.

* SCSF81, Kuraray Company and Bicron B12, Bicron Company

The fibers sticking out at the rear end of the module were bunched together, in the way described before, in two hexagonal structures. They were machine cut and coupled through light guides to photomultipliers (PM) equipped with yellow filters* . The e.m. section was read out by a 1" PM** , the hadronic section by a 2" one*** . Before inserting the fibers, their upstream ends were diamond cut and made reflective by aluminium sputtering, such as to make the response more uniform as a function of the position along the fiber.[16] In order to compensate for the smaller attenuation length of shorter fibers, the fibers starting more than 100 cm from the front face were not aluminized. The calorimeter consists of 19 towers. A central module is surrounded by two rings, arranged in a staggered layout (fig. 1c). The modules were joined together in such a way that a sloping edge of one module always faces an edge that runs parallel to the fibers in the neighboring module (see fig. 1b).

The large lead fraction ($\sim$ 78% of the volume) makes this calorimeter very compact. The effective radiation length (X_0) amounts to 7.2 mm, the effective Molière radius (R_M) 20 mm, the effective nuclear interaction length (λ_I) 21.0 cm[15] and the effective density 9.0 g/cm^3. The depth of the calorimeter corresponds therefore to 9.6 λ_I, laterally it measures about 1.0 λ_I across at the front face, gradually going up to 2.5 λ_I at the back.

This fiber calorimeter was tested in conjunction with another calorimeter, intended to detect the shower leakage. This leakage calorimeter consists of 10 cm thick iron slabs, interleaved with thin-gap wire chambers[17] . In total, there are 8 sampling layers, which makes this calorimeter $\sim$ 4.8 λ_I deep. The thin-gap wire chambers consist of planes of anode wires spaced every 2 mm at a distance of 1.6 mm from two high-resistivity, graphite coated, G10 cathode planes. The anode wires are ganged in groups of 8 to provide a possible anode readout. Behind the cathode planes, two readouts are constructed, one in the form of 1 cm wide strips (not implemented in these tests) and one in the form of 10 $\times$ 10 cm^2 pads. These pads are ganged together across the layers to provide 8-layer deep calorimetric towers. The detector planes were operated at an anode voltage of 3.5 kV with a gas mixture of 55% CO_2 and 45% n-pentane.

To increase the dynamic range of the read-out, the anode signal from each PM was fed into an active splitter, one output of which was sent unchanged into a 12-bit charge ADC, the other output was amplified by a factor $\sim$ 10 before being fed into an ADC. The gain of the PM tubes was set to deliver $\sim$ 4 pC/GeV for the e.m. sections and $\sim$ 12 pC/GeV for the hadronic sections. The ADC gain was 4 counts/pC. The data discussed in this paper were taken at an ADC gate width of 400 ns. Sparse data readout

---

* Kodak Wratten #3

** Philips XP 2961, 8-stage, green extended photocathode

*** Philips XP 2282, 8-stage

was enabled: signals smaller than 4 counts above the pedestal value were not recorded. This corresponds to a cutoff of 25 MeV in the amplified channels of the e.m. sections and 8 MeV for the hadronic channels.

2.2 The beam line

The measurements were performed in the H2 beam line of the SPS at CERN. The calorimeter was mounted on a platform that could move horizontally with respect to the beam line, with a precision of about 1 mm. The detector could also be rotated around its vertical axis, so that the particles could be sent into the detector at a chosen angle θ_z (usually a few degrees) with respect to the fiber axis, in the horizontal plane. And finally, the detector could be rotated around an horizontal axis, running perpendicular to the fibers at a distance of 130 cm upstream from the front face (simulating the beam line in a collider experiment), so that the angle between the particles and the fiber axis remained unchanged when the calorimeter was tilted.

The leakage calorimeter was installed on a fixed platform behind the fiber calorimeter. The distance between the sensitive volumes of the fiber calorimeter and the leakage calorimeter amounted to 80 cm. About 12 cm upstream of the fiber calorimeter, a preshower detector (PSD) was mounted. This detector consisted of an absorber sheet (1.14 X_0 tungsten + 0.53 X_0 lead), followed by a scintillation counter (S6). The signal in the scintillator provided a clean (at energies above 40 GeV about a factor 10) separation between electron and pion events[2] . Further upstream of the calorimeters, a trigger counter telescope was installed. It consisted of 5 scintillation counters (S1 - S5) and 2 drift chambers with x,y readout (BC1, BC2). The layout is shown in fig. 2.

Beams of negative particles of 10, 20, 40, 80 and 150 GeV were sent into the detector at a small angle θ_z with respect to the fiber axis. The beam rates were about 10^3 particles per spill of 2.6 s duration every 14 s. At high energies ($\geq$ 40 GeV) the beams were very clean, the contamination of electrons in the pion beam being below the 1% level. At lower energies this was different. The contaminating electrons (pions) in the pion (electron) beams could be efficiently removed with the help of the PSD data. The pion beams also contained some fraction of muons, which varied from $\sim$ 2% at 150 GeV to $\sim$ 50% at 10 GeV. These muons could be easily recognized and removed from the data samples with the help of the leakage calorimeter (see sect. 3).

2.3 Calibration of the detectors

The e.m. sections of the fiber calorimeter modules were calibrated with 40 GeV electrons. About 2000 electrons were sent into the central region of each of the 19 individual modules, at an angle θ_z of 3^0 with respect to the fiber axis. In this way, on average $\sim$ 92% of the electromagnetic shower energy was deposited in the section

concerned. Off-line, the calibration constants (the relation between picocoulombs and GeV's for each individual tower) could be determined with a statistical precision of $\sim 0.3\%$ from this data. Because of systematic effects, due to fluctuations in the fiber-to-fiber response and in the local sampling fraction, high-voltage instabilities, etc. the tower-to-tower calibration is much less precisely known. We will come back to this point in sect. 4.1.1.

The leakage calorimeter was calibrated with pion beams at energies of 10, 20 and 40 GeV. The calorimeter response was found to be linear in that energy region and the energy resolution was well described as $\sigma/E = 1.2/\sqrt{E(GeV)}$.

Because of the rather complicated segmentation into e.m. and hadronic section, the calibration of the latter was not trivial. Nevertheless, a method, based on the use of high-energy muons was adopted. A narrow beam of muons from the 225 GeV beam was sent into a corner of each module at an angle θ_z of 6^0 with respect to the fiber axis. Because of the small multiple scattering, these muons travel almost in a straight line through the detector. At this angle, they traverse two e.m. and two hadronic sections on their way (fig. 3). The average path lengths in these sections are only determined by geometry and can be exactly calculated. By comparing the average (or the most probable) signals in the e.m. and hadronic sections, one can intercalibrate the latter.

Figure 4 shows typical signal distributions for the four sections traversed by the muons which exhibit clean signals due to the good signal/noise ratio of this type of calorimeter. Even the signals in the first hadronic section, which correspond to an average track length of 12 cm, over which distance the muons lose typically only 0.2-0.3 GeV, are very clean. However, both the lack of uniformity in some of the modules and the small value of the signals in the hadronic sections make the intercalibration between the e.m and hadronic sections rather inaccurate. In the following this intercalibration will be achieved just by normalizing the muon response to the path length, estimating the accuracy of the calibration to be $\simeq 10\%$.

3. EXPERIMENTAL DATA AND METHODS

The results described in the following sections were obtained by analyzing the following sets of data, which were all taken at $\theta_z = 3^0$:

- Electrons of 10, 20, 40, 80 and 150 GeV entering the fiber calorimeter in the central region. Typically, $\sim$ 3000 events were accumulated per run.
- Pions of 20, 40, 80 and 150 GeV entering the fiber calorimeter in the central region. The impact points were displaced horizontally by 2 cm with respect to the electron ones, in order to have the shower maximum, on average, in the central region. Typically, $\sim$ 5000 events were accumulated per run.

- A grid scan, in which 80 GeV electrons were sent into the fiber calorimeter at 25 different impact points, located on a square grid with a period of 1.6 cm, covering an area of 6×6 cm^2 in a rather uniform way. In total, 10^5 events were accumulated. A similar scan (10^5 events) was done at 20 GeV.
- Grid scans for 80 and 20 GeV pions. Here, the grid spacing was 1.5 cm. In total, 10^5 events were accumulated at 80 GeV and 25000 events at 20 GeV.

Clean event samples were produced with the help of the preshower detector and the leakage calorimeter. The PSD allows to remove electron contamination from the pion data sample and vice versa. In practice, the PSD signal was required to be smaller than twice the minimum ionizing value for pions and larger than that for electrons. In the e/π separation analysis, where ultrapure event samples are required, more stringent cuts were applied (see sect. 4.3).

Beam muons were most efficiently removed with the help of the leakage calorimeter, in which muons produce large signals with the characteristic Landau distribution (fig. 5). In the e/π separation studies, any event producing a signal larger than 0.2 GeV in the leakage calorimeter was discarded as a potential muon. For the other topics, where the purity requirements on the data samples are less stringent, muon events were discarded by a cut on the total signal in the fiber calorimeter. This cut was equivalent to 25 % of the incident energy.

Off-line event selection of a single track was done by requiring the pulse height of the scintillation counters S1, S2, S3 to be between 0.5 and 1.7 times the minimum ionizing particle (mip) value. Particles travelling at anomalous angles were removed by requiring that the x and y coordinates measured in the two beam chambers agree within 1 cm. Beam halo particles were removed by cuts on x and y in the beam chambers.

4. EXPERIMENTAL RESULTS

4.1 Electrons

4.1.1 The uniformity of the response

The main concern regarding the performance of this calorimeter applied to the boundary regions between different modules. Since the fibers in the sloping parts of the modules had to be cut perpendicularly to their axis in order to preserve the reflected light component, there is a local deficiency of plastic in these boundary regions, which translates into a smaller sampling fraction and hence a smaller response, compared to the central regions of the towers (see fig. 1d).

This effect was investigated with electron data from the grid scan. Figure 6 shows the average signal from 80 GeV electrons as a function of the impact point of the particles.

Figure 6a shows a horizontal scan of the detector surface, fig. 6b a vertical one. Each point includes electrons hitting the detector in an area with a diameter of 1 mm. The effect described above is clearly observed. In the boundary regions between modules, the response drops by $\sim 10\%$ with respect to the response in the module's center. The beam was steered into the detector at an angle (θ_z) of 3^0 with the fiber axis in these measurements, in the horizontal plane. This explains the fact that the distribution observed in the horizontal scan is skewed, whereas the vertical one is symmetric.

Because of the reproducibility of the effects, one may try to correct for them. This implies, of course, a reasonably precise knowledge of the impact point of the particles, which may either be obtained from external information (in our case the beam chambers), or from the energy sharing between different modules. For the latter method, see sect. 4.1.4. The position dependence of the signals was corrected by multiplying the observed signal by a factor

$$C(x,y) \;=\; \frac{1}{f(x) \times g(y)} \tag{1}$$

where x and y are the coordinates of the impact point, measured with respect to the center of the e.m. section of the calorimeter modules, and f and g are polynomial functions fitted to the data at 80 GeV. The effect of this correction is illustrated by the histograms in fig. 7 for the x scan. Each entry in these histograms represents the average calorimeter signal in an slice of 1 mm, before (fig. 7a) and after (fig. 7b) applying the correction (1). The widths of these distributions are a measure for the signal nonuniformity, which is seen to improve from 3.0% to 0.8% with this procedure. Using the same correction formula at 20 GeV the nonuniformity is reduced from 4.5% to 2%.

4.1.2 Energy resolution and signal linearity

The energy resolution for electrons was studied with particles of 10, 20, 40, 80 and 150 GeV entering the detector at an angle of 3^0 in the horizontal plane. Pure samples of electron data were obtained using the information from the PSD. Particles hitting the calorimeter in the center of the central module deposited $\sim 92\%$ of their shower energy in this module, $\sim 7\%$ was deposited in the six neighboring modules and the rest in the remaining part of the detector. In practice, the signals from all 19 modules, including both EM and HAD sections, were added to obtain the total calorimeter response. The calibration constants measured in the center of each individual module were used for this purpose. The signal distributions were very well described by Gaussian functions. The resolutions in energy were determined from Gaussian fits without any constraint, and are listed in the second column of Table 1.

Because of the large distance from the last bending magnet and because the beam line was sligtly energy dependent, the particles did not hit the calorimeter in the same

area when the energy was changed, this effect being more pronounced at low energy. Therefore, the phenomena discussed in the previous subsection influenced the results significantly. The signals were corrected event-by-event for the position dependent calorimeter response using formula (1). The coordinates of the impact point were derived from the beam chamber information. The results are listed in the third column of table 1 for the energy resolution. As may be expected, the performance improves significantly, especially at low energy.

The energy resolution is graphically shown as a function of the energy in fig. 8. The energy is plotted on a scale linear in $1/\sqrt{E}$. It is clear that, apart from a term scaling as $1/\sqrt{E}$, there is an energy independent contribution to the energy resolution. Two fits were performed, whose results also shown in the figure, are :

$$\frac{\sigma}{E} = \frac{(12.74 \pm 0.46)\%}{\sqrt{E(GeV)}} + (1.94 \pm 0.02)\% \qquad (\chi^2 = 5/\text{d.o.f.}) \qquad (2a)$$

$$\frac{\sigma}{E} = \frac{(17.49 \pm 0.03)\%}{\sqrt{E(GeV)}} \oplus (2.70 \pm 0.01)\% \qquad (\chi^2 = 2.8/\text{d.o.f.}) \qquad (2b)$$

The results of these fits are slightly worse (for the constant term) than those published by Acosta et al.[9] for their nonprojective calorimeter.

The average calorimeter response, normalized to 1 at 40 GeV, is listed in the last column of Table 1, and is shown as a function of the electron energy in fig. 9. Nonlinearities are at the 2 % level.

4.1.3 Light yield

The e.m. energy resolution is ultimately limited by the purely statistical fluctuations in the number of charge carriers constituting the signals. Since this number is proportional to the energy, the resolution of this calorimeter can be expressed by

$$\frac{\sigma}{E} = \frac{\sqrt{\sigma^2_{\text{samp}} + \sigma^2_{\text{p.e.}}}}{E} + c \qquad (3)$$

where σ_{samp} describes the sampling fluctuations and $\sigma_{\text{p.e.}}$ the fluctuations due to photoelectron statistics. The contribution of the latter term was determined by measuring the effect of a reduction of the light yield, by means of neutral filters, on the total energy resolution σ/E. The measurements were done at low energy (10 GeV), in order to limit the contribution of the energy independent term c to the resolution as much as possible. The energy resolutions and the average signals obtained with a single module and with different filters are listed in table 2.

Since the number of photoelectrons, $N_{\text{p.e.}}$, is equal to $(\sigma_{\text{p.e.}}/E)^{-2}$, (3) can be rewritten as

$$(\frac{\sigma}{E} - c)^2 \;=\; (\frac{\sigma_{\text{samp}}}{E})^2 \;+\; \frac{1}{f.N_{\text{p.e.}}} \tag{4}$$

where f is fraction of light passing the filter. Figure 10 shows the quantity $(\sigma/E - c)^2$ for $c = 2\%$ as a function of the average signal, plotted on a scale proportional to its inverse. Indeed, a linear relationship is observed, from which the number of photoelectrons and the sampling term could be determined. The average number of photoelectrons produced per GeV shower energy (in the absence of neutral filters) amounts to 470 ± 25. This value is corrected for the shower containment in a single module. The error is mainly determined by the uncertainty in the contribution of the energy independent term c (see also sect. 4.1.2).

4.1.4 Position resolution

The position resolution was determined from the energy sharing between the different calorimeter modules. The center of gravity $(\bar{x}, \bar{y})$ of the energy E_i deposited in the various calorimeter modules (located at positions (x_i, y_i) with respect to the calorimeter center) contributing to the signal was calculated as

$$\bar{y} \;=\; \frac{\sum_i y_i E_i}{\sum_i E_i} \tag{5}$$

and similarly for the $\bar{x}$ coordinate. It is well known that the impact point calculated in this way tends to be systematically shifted toward the center of the module hit by the particle[13,18,19,20]. This is illustrated in fig. 11a, in which the $\bar{y}$ coordinates are compared to the real impact points, given by the y_{BC} coordinates derived from the beam chamber data. Only in the module center and near the boundaries between different modules the impact point is correctly determined.

One may solve this problem either by giving a larger weight to modules with a small energy deposit in calculating the center of gravity, or by shifting the center of gravity found by (5) using an empirical algorithm. The latter procedure was chosen in this analysis. The reconstructed impact point $(\bar{x}, \bar{y})$ was shifted to the approximately correct position in the following way:

$$\bar{y}_{\text{corr}} \;=\; 13.8 \;\arctan(0.42\bar{y}) \;\text{ mm} \tag{6}$$

The relation between the real impact points y_{BC} and the reconstructed ones $\bar{y}_{\text{corr}}$ is shown in fig. 11b. The points in this scatter plot cluster around the line $y_{\text{BC}} = \bar{y}_{\text{corr}}$, which shows that the method works well. The experimental data entering the scatter

plots of fig. 11 were taken from the grid scan at 80 GeV, where the central detector module was rather uniformly covered with electron hits. Similar data were taken at 20 GeV. The correction formula (6) works equally well at this energy.

The position resolution is given by the width of the band in fig. 11. This resolution is clearly position dependent, as illustrated in fig. 12. The best resolution, ~ 0.5 mm, is observed near the boundaries between modules. In the center of a module, the resolution deteriorates to ~ 1 mm. The same tendency was also observed at 20 GeV. For other energies, only data in the vicinity of the center of the calorimeter were available. The position resolution in this area is shown as a function of energy in fig. 13. This data is adequately described by the following expression

$$\sigma_y = \frac{7.5\text{mm}}{\sqrt{E(GeV)}} \tag{7}$$

after unfolding of the beam chambers resolution ($\simeq 430$ μm). As pointed out before, the *average* position resolution of this calorimeter is about 50% better than this. These results may be compared to the 17.1 mm/$\sqrt{E(GeV)}$ found by Acosta et al., for a calorimeter with the same composition, but with a cell size of 48.7 cm^2, i.e. with an effective diameter of 3.9 R_M. Our result confirms the intuitive expectation that the position resolution is approximately proportional to this effective diameter (or the square root of the cell size).

For the x coordinate, a similar resolution as in (7) was found, plus a constant term $\simeq 0.4$ mm coming from the fluctuations in depth of the shower development. Assuming a fluctuation of $\simeq 1X_0$ to first order energy independent, and for an incident angle of 3 degrees this gives 0.37 mm, in good agreement with what was measured.

4.2 Pions

The detector is not sufficiently large to contain hadronic showers. Therefore, no effort was made to study the hadronic performance in great detail. Instead, we focused our attention on those issues that are specific for the modularity and the projectivity of the calorimeter. The virtues of the projectivity are discussed in section 4.3. In sect. 4.2.1, the consequences of the modularity are investigated.

4.2.1 Signal uniformity

In sect. 4.1.1, the modularity, and in particular the local decrease in the sampling fraction occurring near the interface between modules, was seen to cause a considerable signal nonuniformity for e.m. showers. This problem was investigated also for hadronic

showers. The data from the pion grid scans were used for this purpose. The total calorimeter signal was obtained by adding the signals from all 19 e.m. and all 19 hadronic module sections. For the signals from the e.m. sections, the calibration constants obtained by shooting electrons in the center of each module were used and for the hadronic sections those derived from the muon runs (see sect. 2.3).

In fig. 14, the results of a horizontal (fig. 14a) and a vertical (fig. 14b) scan with 80 GeV π^- around the center of the calorimeter are given. Pions showers are considerably wider than e.m. ones and, therefore, local nonuniformities in the detector structure, on a scale of a few mm, should have smaller effects on the uniformity of the pion signals than for the e.m. ones. The differences between the results from the horizontal and vertical scans may be understood from the fact that the particles enter the detector at an angle of 3^0 in the *horizontal* plane. The starting points of the pion showers fluctuate on a scale of about 30 cm in depth (one pion interaction length[13]), which translates in a lateral smearing with a σ of $\sim$ 16 mm (40% of the diameter of a module), for pions with the same impact point. Such a smearing does not occur in the vertical plane. Figure 14 does show the effects of incomplete shower containment. The average signal gradually decreases when the beam moves away from the center of the calorimeter. Because of the 3^0 angle, the optimal containment in the horizontal scan is achieved for an impact point which is $\sim$ 3 cm off-center. This effect appears to have the same magnitude as for electrons. It is nevertheless very sensitive to the accuracy of the intercalibration between electromagnetic and hadronic sections. Moreover the shape of the observed response is reproducible and can be corrected easily.

This analysis was repeated for the 20 GeV data (fig. 15). The conclusions are very similar, albeit that the boundary effects are less pronounced than at 80 GeV. This may be understood from the fact that the narrow e.m. core, caused by π^0 production in the hadronic shower development is less pronounced at low energy[5] .

4.2.2 Energy resolution and lateral shower containment

The energy resolution and the lateral shower containment were studied with 10, 20, 40, 80 and 150 GeV pions entering the calorimeter in its central region at an angle of 3^0 to the fiber axis. The total calorimeter signal was determined as described in the previous subsection. The signal distributions were fitted to Gaussian functions, in an unconstrained way. The average signals and the energy resolutions obtained from these fits are listed in table 3.

Since signals from electrons are much more affected by nonuniformities in the sampling fraction (see sections 4.1.1 and 4.2.1), which are smeared out in the hadronic signal distributions, one needs to average the e.m. response over the calorimeter surface for such a comparison. From the data shown in fig. 6, and from similar data taken at 20 GeV, we conclude that this average response is $\sim$ 5% lower than the value found in the

center of the calorimeter. The average electron signals, taken from table 2 and corrected for this effect, are listed in table 3. The e/π signal ratios, which can be calculated from this data, and which are also listed in the table, may be compared to the e/π signal ratios determined for a much larger detector with the same composition[9] , in order to estimate the average fraction of the lateral energy leakage. The results of this exercise are listed in the last column of table 3. It turns out that the calorimeter contains 70-75% of the hadronic shower, depending on the energy. Because of the increased fraction of π^0 production, high-energy showers are better contained than low-energy ones, in agreement with previous observations[5] .

The energy resolution is shown as a function of the energy in fig. 16. The experimental results are well described by

$$\frac{\sigma}{E} = \frac{(49.6)\%}{\sqrt{E(GeV)}} + (6.5)\% \tag{8}$$

Of course, the energy resolution is considerably affected by the incomplete shower containment. Acosta et al.[9] studied the effects of side leakage on the hadronic energy resolution and parametrized these as

$$\frac{\sigma}{E} = \sqrt{(\frac{c_1}{\sqrt{E}})^2 + (\frac{f_{\mathrm{leak}}}{\sqrt[4]{E}})^2} + c_2 \tag{9}$$

When using our values for the leakage fraction f_{leak}, we find that our data are best described by an expression of this type when $c_1 = 35.3\%$ and $c_2 = 1.8\%$. The resulting fit is also shown in fig. 16. These values are in good agreement with the ones published in ref. 9.

4.3 Electron-pion separation

The segmentation into an e.m. and an hadronic section, albeit not in the explicit longitudinal way that one is used to, opens up new possibilities for recognizing electrons. These possibilities were already exploited during the data taking. Electron-pion separation studies require ultrapure beams to start with. In the beam line used for the tests, the electron contamination in the pion beams is, among other things, determined by the thickness of a lead absorber placed far upstream, just beyond the pion production target. The thickness of the mentioned absorber was carefully chosen in such a way that no significant electron contamination occurred, while maintaining an acceptable particle rate, pions being multiply scattered by the absorber. Electron contamination was immediately recognized on-line since these particles, unlike pions, deposit almost 100% of their energy in the e.m. calorimeter section.

Dedicated e/π separation studies were performed at 20 and at 80 GeV, using the grid scan data. Therefore, the results that are obtained do not refer to any specific impact point, but they are typical for the calorimeter as a whole. Since very small effects are being investigated, the purity of the data samples is absolutely crucial. As already pointed out, the purity of the beam itself was optimized by choosing an appropriate absorber thickness. Off-line, hard cuts were applied using the data from the PSD and the leakage calorimeter. Any event showing a significant signal in the leakage calorimeter was discarded as a potential muon. Pions were only retained if the signal in the preshower detector was in between 0 and 1 times the most probable value for a minimum ionizing particle, for electrons a PSD signal of at least 6.7 times that value was required. After these cuts, the data samples contained 45551(13617) electrons of 80 (20) GeV and 34859(9672) pions of 80 (20) GeV.

Figure 17 shows distributions of the ratio of the energy deposited in the hadronic and e.m. calorimeter sections, $E_{\rm had}/E_{\rm e.m.}$, for the 80 GeV electron and pion events. A very clear distinction between these two distributions is observed. The e/π separation that can be achieved using this information is given in fig. 18, where the fractions of electrons and pions passing a cut $E_{\rm had}/E_{\rm e.m.} < f_{\rm cut}$ are shown as a function of $f_{\rm cut}$. For example, only 3 out of 1000 pions deposit less than 1% of their energy in the hadronic calorimeter section, while more than 95% of the electrons pass such a cut. At 20 GeV, the results were clearly worse. At 92% electron efficiency, 4% of the pions were misidentified.

Apart from the energy sharing between the e.m. and hadronic calorimeter sections, also the differences in the lateral shower profiles of e.m. and hadronic showers may be exploited. This method was extensively studied by Acosta et al.[13] , who achieved e/π separation at a level comparable to the one shown in fig. 18, using lateral shower information alone. A quantity R_p was defined :

$$R_p = \frac{\sum_i r_i E_i^{0.4}}{\sum_i E_i^{0.4}} \tag{10}$$

where E_i is the energy deposited in an individual module i and r_i the distance between the center of this module and the center of gravity of the energy deposit profile, calculated with (5). All 19 towers were used for calculating R_p. Electrons and pions are clearly separated using this parameter, which is a measurement of the effective shower width (fig. 19).

In order to investigate the combined effect of the two methods, the latter one was applied on samples of events that deposited less than 1% of their energy in the hadronic calorimeter section (see fig. 18). The R_p distributions for the 80 GeV electrons and pions fulfilling this condition are given in fig. 20. Clearly, the e/π separation is considerably improved if the lateral shower information is included. Figure 21 shows the

e/π separation results achieved when both the energy sharing between the e.m. and hadronic calorimeter sections and the lateral energy deposit profile are taken into consideration. The cuts on $E_{\rm had}/E_{\rm e.m.}$ (< 0.01) and R_p (< 3.8) can be chosen in such a way that at 80 GeV less than 1 out of 1000 pions are misidentified as electrons, for an electron efficiency of $> 95\%$.

4.4 Shower leakage

In the analyses described in the previous subsections, events that were longitudinally contained in the $9.6\lambda_I$ deep fiber calorimeter were selected by discarding events depositing more than 0.2 GeV in the leakage calorimeter. In this subsection, the information provided by this leakage calorimeter is studied.

First, we investigated to what extent the shower leakage information can be used to improve the hadronic energy resolution. The 80 GeV pion events from the grid scan were used for this purpose. The muons contaminating the beam ($\sim 2\%$ of the events) were eliminated by requiring that the total energy deposited in the fiber calorimeter be larger than 20 GeV. In fig. 22, the signal measured in the fiber calorimeter is plotted versus the signal in the leakage calorimeter. A clear correlation between these signals is observed. This correlation leads to a significant improvement in the total energy resolution when both signals are added (fig. 23). The leakage calorimeter is particularly useful to improve the measurements on showers starting deep inside the calorimeter. This is illustrated in fig. 24, where the average leakage calorimeter signal is given as a function of the fraction of the shower energy deposited in the hadronic calorimeter section. Late showers deposit a large fraction of their energy in the hadronic section.

Detailed analysis of the leakage calorimeter data itself provides interesting information on the type of particles escaping from the fiber calorimeter. Based on the pattern of the energy deposit, one can distinguish between soft neutrons, muons and hadrons. A muon traversing the leakage calorimeter deposits at least 1 GeV in it (see fig. 5). Signals smaller than that are almost exclusively due to soft neutrons. The signals are almost always totally confined to only one calorimeter tower in this case. Escaping hadrons cause showers in the leakage calorimeter. The shower energy is usually shared between several towers. In some cases, escaping hadrons may carry a considerable fraction of the total shower energy : this has to be expected, since about 1 out of 1000 pions will traverse the whole fiber calorimeter without causing even a single nuclear reaction.

Muons may be produced in the hadronic shower when secondary pions or kaons decay in flight. Such muons give a very characteristic signal in the leakage calorimeter (see fig. 5). The signal from the muon track is confined to only one or two towers. In fig. 25, the leakage signal distribution is given for events depositing more than 30 GeV in the fiber calorimeter and for which more than 95% of the leakage signal is carried by the

central towers. This signal distribution shows indeed the characteristic Landau shape. It seems that in a significant fraction of the events *two* muons are produced. When the signal distribution is unfolded into two Landau distributions, one with a shape given by the beam muon measurements (fig. 5) and the other obtained by convoluting the latter one with itself, a good description of the experimental data is obtained. From this, we conclude that the rate of dimuon production relative to the rate of single muon production amounts to

$$\frac{N(\mu\mu)}{N(\mu)} = 0.061 \pm 0.023 \tag{11}$$

Muon production in hadronic shower development was studied before by Acosta et al.[4] for a fiber calorimeter with the same composition. At 80 GeV, the rate of μ production was measured to be $\sim$ 1.2%. If pion/kaon decay in flight would be the only source of such muons, there would be no reason to expect the $\mu\mu$ production to be larger than 1.2% of the single μ rate. The fact that a larger dimuon production is observed must, therefore, mean that most of these dimuons are produced by a different mechanism. A likely candidate for such a mechanism is ρ^0 decay. The process $\rho^0 \rightarrow \mu\mu$ has a branching ratio of 0.0067%. These ρ^0's are presumably abundantly produced in hadronic showers and the observed level of $\mu\mu$ production seems compatible with this hypothesis.

5. SUMMARY AND CONCLUSIONS

We have studied the performance of a modular, fully projective lead calorimeter with 1 mm thick scintillating plastic fibers sampling the showers. The lead to fiber ratio was 4:1 which yields a very compact and almost compensating detector. The modularity and the projectivity offer advantages and disadvantages compared to a non-modular and nonprojective device tested by Acosta et al.. The fibers that start at some depth inside the calorimeter cause a local decrease in the sampling fraction near the interfaces between modules, resulting in a significantly smaller response for narrow (electromagnetic) showers developing in these regions. Knowing the impact point of the particles, one can efficiently correct the signals for this effect. The knowledge of the impact point (position resolution) benefits considerably from the cell size, the projectivity yielding a granularity much better adapted to the natural lateral dimensions of the electromagnetic and hadronic showers. For electrons, we measured a position resolution of 7.5 mm/$\sqrt{E(GeV)}$ in the cell center. The energy resolution for electrons was found to be 12.7%/$\sqrt{E(GeV)}$ + 1.9%, and the light yield of the calorimeter amounts to $\sim$ 470 photoelectrons/GeV.

Nonuniformities near the module boundaries played a smaller role for the much broader pion showers. Pions deposited on average 75% of their energy in this rather

narrow detector. When corrected for the effects of lateral leakage, the hadronic energy resolution was found to be in agreement with the performance of a sufficiently large calorimeter with the same composition.

Thanks to the projectivity, an effective segmentation into an e.m. and hadronic calorimeter section could be achieved, in spite of the monolythic module structure, by separating the readout of the fibers running throughout the calorimeter from those starting at a depth beyond $\sim$ 25 radiation lengths. We demonstrated that these two sections could be crudely intercalibrated with muons. This segmentation into an e.m. and an hadronic section provided about two orders of magnitude in e/π separation. When, in addition, the lateral shower information was used, one more order of magnitude was gained.

The $9.6\lambda_I$ deep fiber calorimeter was tested in conjunction with a backing calorimeter consisting of thin-gap wire chambers, interleaved by thick iron slabs. The shower leakage information provided by this detector improved the energy resolution for late starting hadron showers. Analysis of the shower leakage data revealed that the hadron calorimeter generates dimuons at an unexpected high rate, which may be due to the process $\rho \rightarrow \mu\mu$.

Acknowledgements

The work described in this paper would have been impossible without the outstanding technical support provided by our engineers and technicians M. Billault, S. Bricola, B. Canton, J.-M. Chapuis, J-C. Clémens, P. Clément, M. Commerçon, F. Daudon, J-J. Destelle, C. Farella, B. Foligne, A. Freddi, R. Gorini, D. Imbault, G. Improta, G. Iuvino, P. Laloux, S. Mayade, F. Pagano, R. Pirard, P. Repain, R. Rocco, L. Rose-Dulcina, D. Sauvage, G. Savinel, and C. Schillinger. Financial support from the Istituto Nazionale di Fisica Nucleare to the Napoli and Pavia groups, from the Junta Nacional de Investigaçao Cientifica of Portugal to the Lisbon group, from the Conselho Nacional de Desenvolvimento Cientifico e Tecnologico of Brazil to the Rio de Janeiro group, and from the Institut National de Physique Nucléaire et de Physique des Particules is acknowledged. One of us (F.R.) would like to thank the Digital Equipment Corporation for support. And finally, we are grateful to the staff of the SPS, and in particular to N. Doble, for the excellent beam conditions and assistance provided during our tests.

REFERENCES

1. F.G. Hartjes and R. Wigmans, Nucl. Instr. and Meth. **A277** (1989) 379.
2. D. Acosta *et al.*, Nucl. Instr. and Meth. **A302** (1991) 36.
3. D. Acosta *et al.*, Nucl. Instr. and Meth. **A314** (1992) 432.
4. D. Acosta *et al.*, Nucl. Instr. and Meth. **A309** (1991) 143.
5. D. Acosta *et al.*, Nucl. Instr. and Meth. **A316** (1992) 184.
6. D. Acosta *et al.*, Nucl. Instr. and Meth. **B62**(1991), 116.
7. A. Simon (WA89 Collaboration), Detecting and triggering on neutrons using the SPACAL Pb/scintillating-fiber calorimeter, contribution to the 2nd Int. Conf. on Calorimetry in High Energy Physics, Capri (I), 1991.
8. R. Wigmans, Nucl. Instr. and Meth. **A259** (1987) 389.
9. D. Acosta *et al.*, Nucl. Instr. and Meth. **A308** (1991) 481.
10. The GEM Collaboration, Letter of Intent for an Experiment at the SSC (1991).
11. The ATLAS Collaboration, Letter of Intent for an Experiment at the LHC (1992).
12. The CMS Collaboration, Letter of Intent for an Experiment at the LHC (1992).
13. D. Acosta *et al.*, Nucl. Instr. and Meth. **A305** (1991) 55.
14. D. Acosta *et al.*, Nucl. Instr. and Meth. **A320** (1992) 128.
15. We define the nuclear interaction length λ_I in the same way as the Particle Data Group in Phys. Lett. **B239** (1990), page III 5,6. It is the mean free path for *protons* between inelastic interactions. Since the inelastic cross sections for pions are $\sim 50\%$ larger, $\lambda_\pi \approx 1.5\lambda_I$.
16. D. Acosta *et al.*, Nucl. Instr. and Meth. **A294** (1990) 193.
17. S. Majewski *et al.*, Nucl. Instr. and Meth. **217** (1983) 265; G. Bella *et al.*, Nucl. Instr. and Meth. **A252** (1986) 503; S. Dado *et al.*, Nucl. Instr. and Meth. **A252** (1986) 511; G. Mikenberg, Nucl. Instr. and Meth. **A265** (1988) 223.
18. G.A. Akopdjanov *et al.*, Nucl. Instr. and Meth. **140** (1977) 441.
19. R.L. Carrington *et al.*, Nucl. Instr. and Meth. **163** (1979) 203.
20. S. Orito and T. Kobayashi, Nucl. Instr. and Meth. **215** (1983) 93.

FIGURE CAPTIONS

1. The structure of the fiber calorimeter. Shown are a detail of the calorimeter's front face (a), a schematic impression (not to scale) of the longitudinal cross section of two neighboring modules (b), the modular structure seen by the particles entering the detector (c) and a detail of the sloping edge (d).
2. Layout of the beam line, seen from above. In our convention, the angle θ_z shown in this figure has a positive sign. See text for details.
3. Intercalibration of the e.m. and hadronic calorimeter sections with muons at 6^0. The muon trajectories in the first e.m., the first hadronic, the second e.m. and the second hadronic section are 42.5, 12.1, 60.7 and 75.6 cm long, respectively. See text for details (drawing not to scale).
4. Typical distributions of the calibration signals obtained from 225 GeV muons traversing the first e.m. (a), the first hadronic (b), the second e.m. (c) and the second hadronic (d) section at $\theta_z = 6^0$ (cf. fig. 3).
5. The signal distribution for 80 GeV beam muons traversing the leakage calorimeter.
6. The average calorimeter signal for 80 GeV electrons as a function of the impact point. Shown are the results for a horizontal (a) and a vertical (b) scan of the detector surface. The boundaries between the different detector modules are indicated by arrows. The electrons entered the detector in the horizontal plane at an angle $\theta_z = 3^0$ with respect to the fiber axis.
7. The nonuniformity of the electron signals. Each entry in the histograms represents the average calorimeter signal for 80 GeV electrons, measured in a slice of 1 mm. Results are given before (a) and after(b) correcting for the position dependence of the calorimeter signals. Data taken at $\theta_z = 3^0$.
8. The energy resolution for electrons as a function of energy, for $\theta_z = 3^0$. The dashed (resp. dotted) is the result of a linear (resp. quadratic) fit to the experimental data.
9. The average calorimeter signal per unit of energy, normalized to 1 at 40 GeV, for electrons entering the detector at an angle $\theta_z = 3^0$. The signals were corrected for the position dependence of the calorimeter response (see text).
10. The scaling term of the energy resolution for 10 GeV electrons as a function of the average calorimeter signal, obtained from measurements with different neutral filters. The abcissa is linear in the inverse of the signal. A value of 2% for the contribution of the energy independent term c is used.
11. Scatter plots for 80 GeV electrons, showing the y-coordinate of the impact point measured with the beam chambers versus the y-coordinate determined from the

calorimeter data with the center-of-gravity method. Results are shown before (a) and after (b) correcting for the systematic displacement effects inherent to this method, with formula (6). Data taken at $\theta_z = 3^0$.

12. The position resolution for 80 GeV electrons as a function of the y coordinate of the impact point, for $x \approx 0$. Data taken at $\theta_z = 3^0$.

13. The position resolution for electrons at $\theta_z = 3^0$ as a function of energy, for particles entering the calorimeter in the central region of a module. Averaged over the whole detector, the results are $\sim 50\%$ better.

14. The average calorimeter signal for 80 GeV pions as a function of the impact point. Shown are the results for a horizontal (a) and a vertical (b) scan of the detector surface. The boundaries between the different detector modules are indicated by arrows. The pions entered the detector in the horizontal plane at an angle $\theta_z = 3^0$ with respect to the fiber axis.

15. The average calorimeter signal for 20 GeV pions as a function of the impact point. Shown are the results for a horizontal (a) and a vertical (b) scan of the detector surface. The boundaries between the different detector modules are indicated by arrows. The pions entered the detector in the horizontal plane at an angle $\theta_z = 3^0$ with respect to the fiber axis.

16. The energy resolution for pions entering the calorimeter in its central region at an angle of 3^0. The lines are the results of best fits to the experimental data. See text for details.

17. Distributions of the ratio of the energy deposited in the hadronic and the e.m. calorimeter sections, for electrons and pions of 80 GeV.

18. Electron-pion separation at 80 and 20 GeV. Shown are the fractions of electrons (a) and pions (b) that pass a cut $E_{\rm had}/E_{\rm e.m.} < f_{\rm cut}$, as a function of $f_{\rm cut}$.

19. Distribution of the effective width R_p of 80 GeV electron and pion showers. Data taken at $\theta_z = 3^0$.

20. Distribution of the effective shower width R_p for 80 GeV electrons and pions depositing less than 1% of their energy in the hadronic calorimeter section.

21. Electron-pion separation at 80 GeV. Shown are the fractions of electrons (a) and pions (b) that deposit less than 1% of their energy in the hadronic calorimeter section and have an effective shower width R_p smaller than $R_p^{\rm cut}$, as a function of $R_p^{\rm cut}$.

22. Scatter plot for 80 GeV pions, showing the signal in the leakage calorimeter versus the signal in the fiber calorimeter.

23. Comparison of the signal distributions for 80 GeV pions measured by the fiber calorimeter alone (a) and by the fiber and the leakage calorimeters combined (b).

24. The average signal in the leakage calorimeter as a function of the fraction of the shower energy deposited in the hadronic calorimeter section. Data for 80 GeV pions.

25. The signal distribution in the leakage calorimeter for events in which muons are produced in 80 GeV pion showers developing in the fiber calorimeter. The dotted line represents the Landau response for one muon, the dashed one the response to a second muon, and the solid one the response for two produced muons.

TABLE CAPTIONS

1. Energy resolution and signal linearity for electrons. Listed are the beam energy, the energy resolution as measured from the raw data, the energy resolution obtained after correcting for the position dependent calorimeter response and the average signal per unit of energy, normalized to 1 at 40 GeV.
2. Determination of the light yield of the calorimeter. Listed are for each neutral filter the measured transmission coefficient f, the energy resolution for 10 GeV electrons, the average calorimeter signal for the detection of these particles, and the squared energy resolution obtained after subtracting the energy independent term c. For the latter, we chose a value of 2%.
3. Energy resolution and shower containment for pions. Listed are the beam energy, the average signals for electrons and pions, the e/π signal ratio and the average fraction of lateral energy leakage. The latter result is based on the assumption that the e/h value amounts to 1.15.

Table 1 Electron resolution and linearity			
E (GeV)	$(\sigma/E)_{\text{meas}}(\%)$	$(\sigma/E)_{\text{corr}}(\%)$	<signal/E>
9.6	6.60±0.13	6.40±0.13	1.018±0.002
20	5.00±0.08	4.60±0.07	1.012±0.001
40	4.10±0.07	3.80±0.07	1.000
80	3.40±0.06	3.40±0.06	1.023±0.001
150	3.00±0.06	3.00±0.06	1.016±0.001

Table 2 Light yield				
Filter	f_{measured}	σ/E (%)	<Signal> (pC)	$(\sigma/E - 0.02)^2 \times 10^4$
NO	1	7.39±0.1	38.002±0.002	29.05±1.
1	0.260	7.75±0.2	9.881±0.002	33.±2.
2	0.154	8.48±0.1	5.867±0.002	42.±1.
3	0.041	11.3±0.2	1.575±0.003	86.±4.

Table 3 Pion resolution and e/π signal ratio					
E (GeV)	$<\text{signal}>_e$ (pC)	$<\text{signal}>_\pi$ (pC)	$(\sigma/E)_\pi$ (%)	e/π	$< f_{\text{leak}} >$ (%)
20	84.5±0.05	53.8±0.2	17.4±0.3	1.57±0.01	29.5
40	176.1±0.2	115.1±0.4	14.4±0.25	1.530±0.005	29.3
80	368.6±0.3	243.1±0.7	12.4±0.2	1.510±0.004	29.2
150	681.2±0.6	474.2±1.1	10.3±0.15	1.440±0.003	26.2

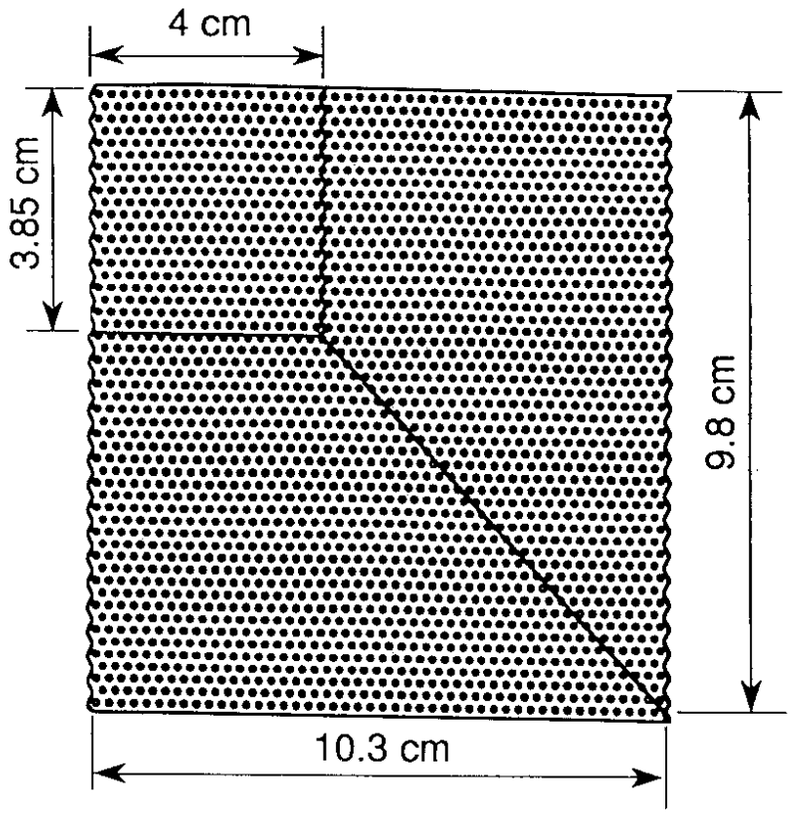

a)

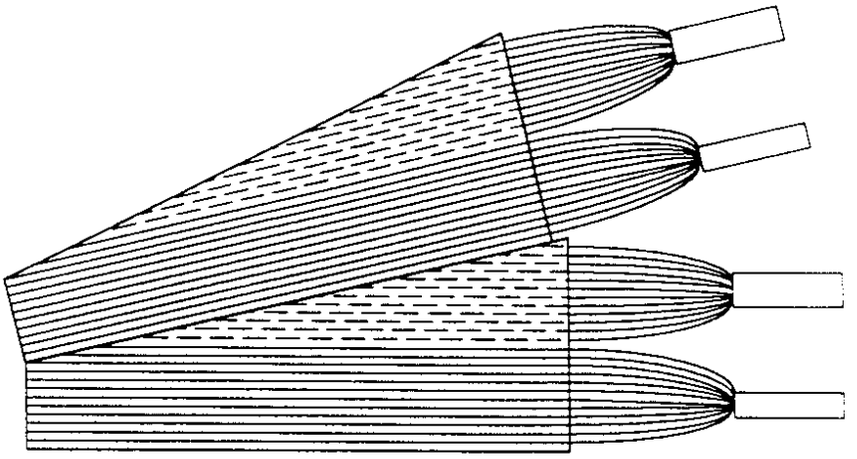

b)

c)

d)

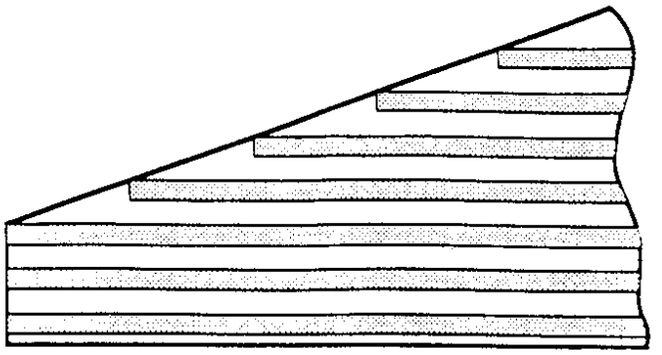

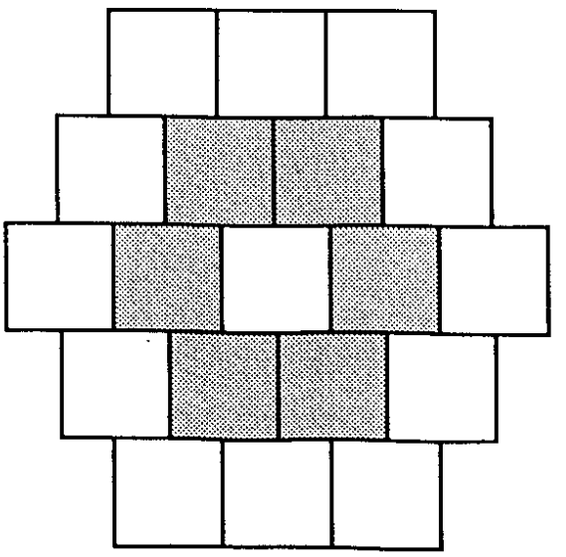

Fig. 1

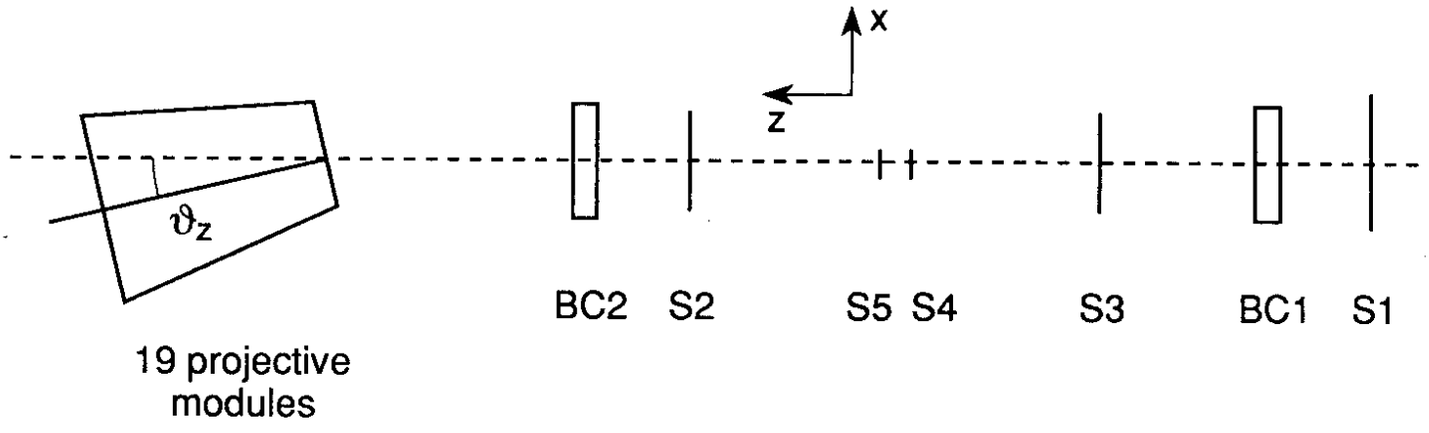

Fig. 2

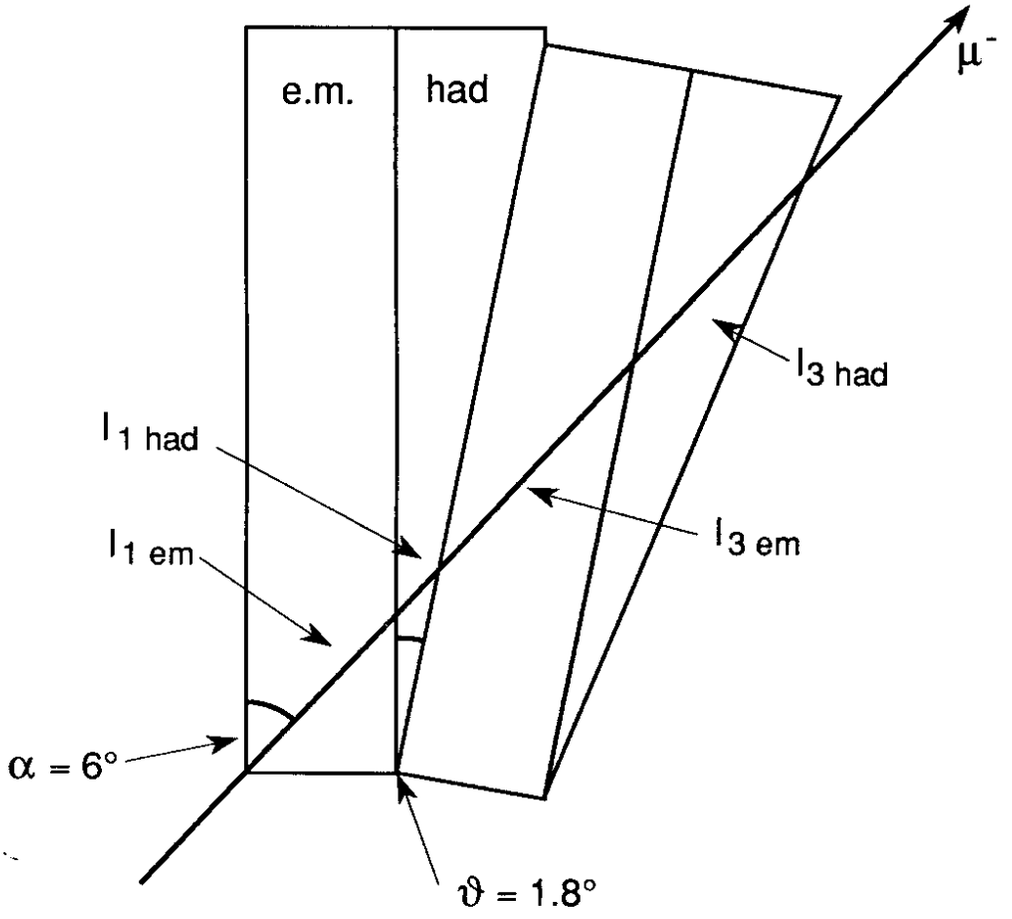

Fig. 3

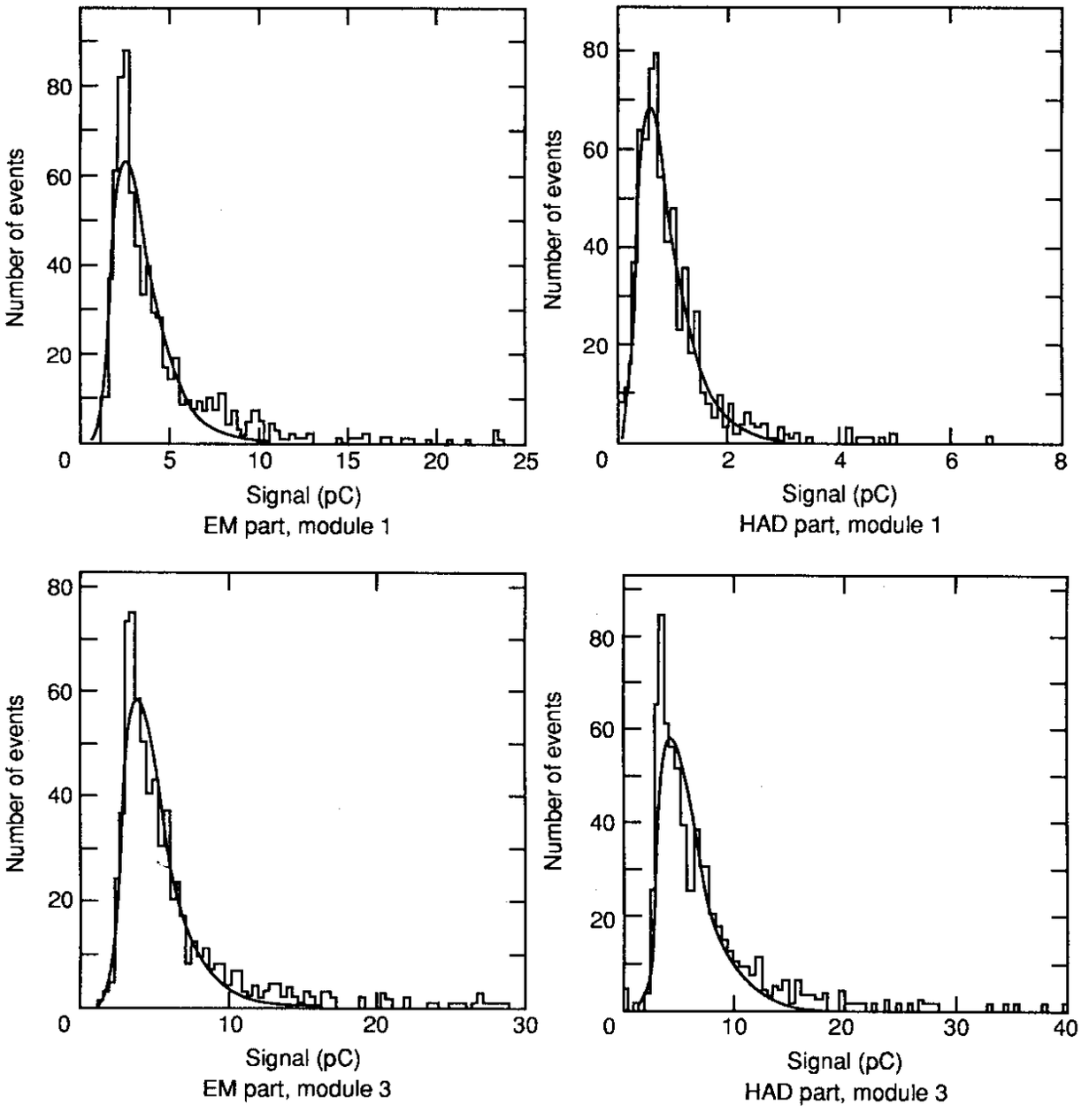
Number of events
Signal (pC)
EM part, module 1
HAD part, module 1
EM part, module 3
HAD part, module 3

Fig. 4

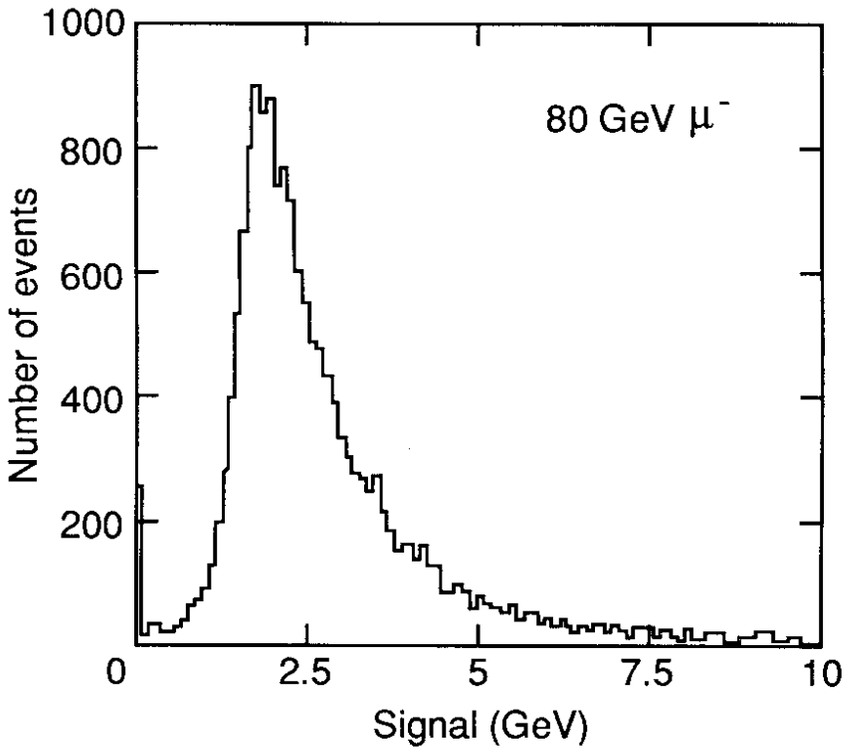
1000
800
600
400
200
0
2.5
5
7.5
10
Number of events
Signal (GeV)
80 GeV μ⁻

Fig. 5

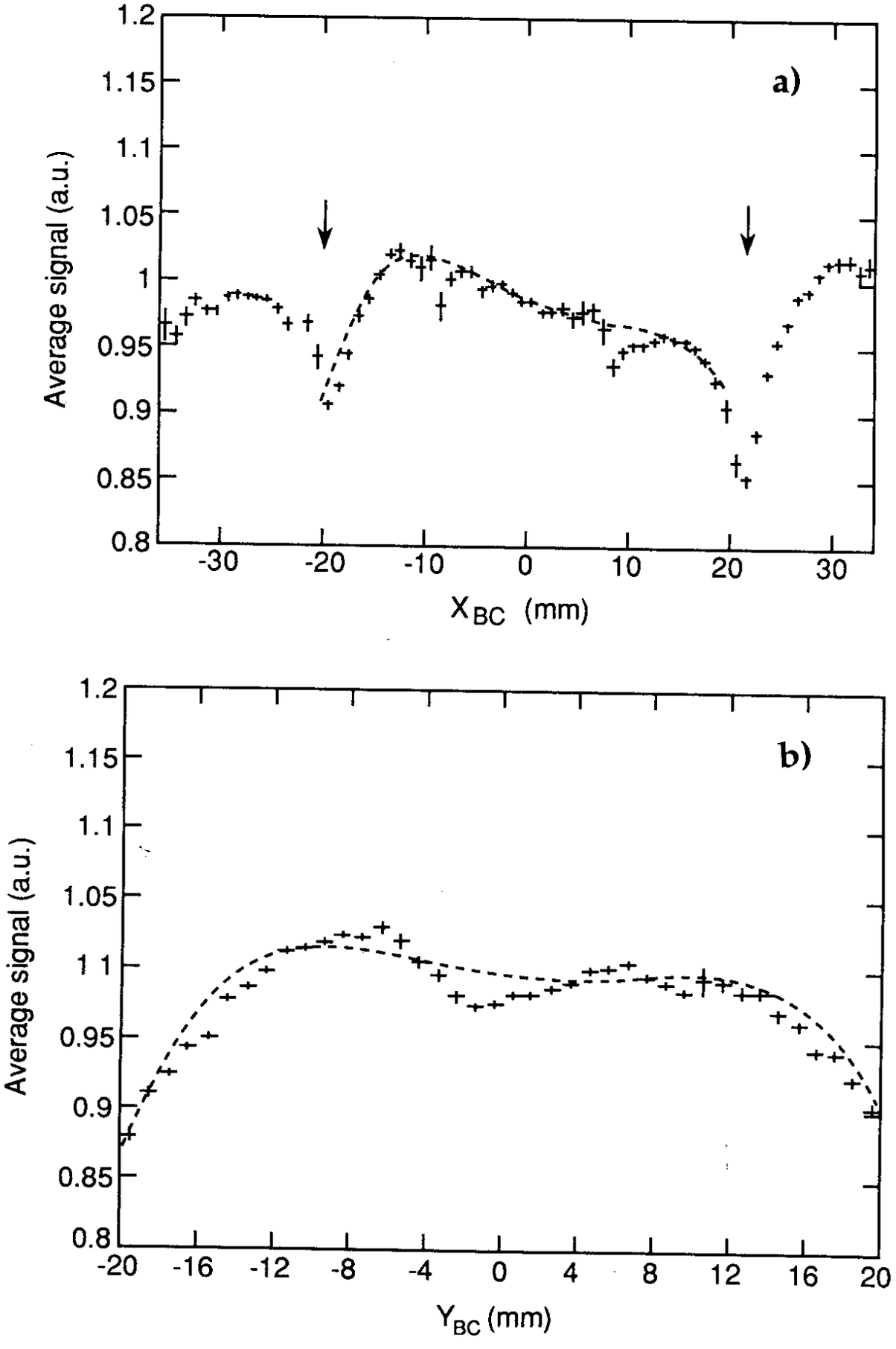
a)
Average signal (a.u.)
1.2
1.15
1.1
1.05
1
0.95
0.9
0.85
0.8
-30
-20
-10
0
10
20
30
X_{BC} (mm)
b)
Average signal (a.u.)
1.2
1.15
1.1
1.05
1
0.95
0.9
0.85
0.8
-20
-16
-12
-8
-4
0
4
8
12
16
20
Y_{BC} (mm)

Fig. 6

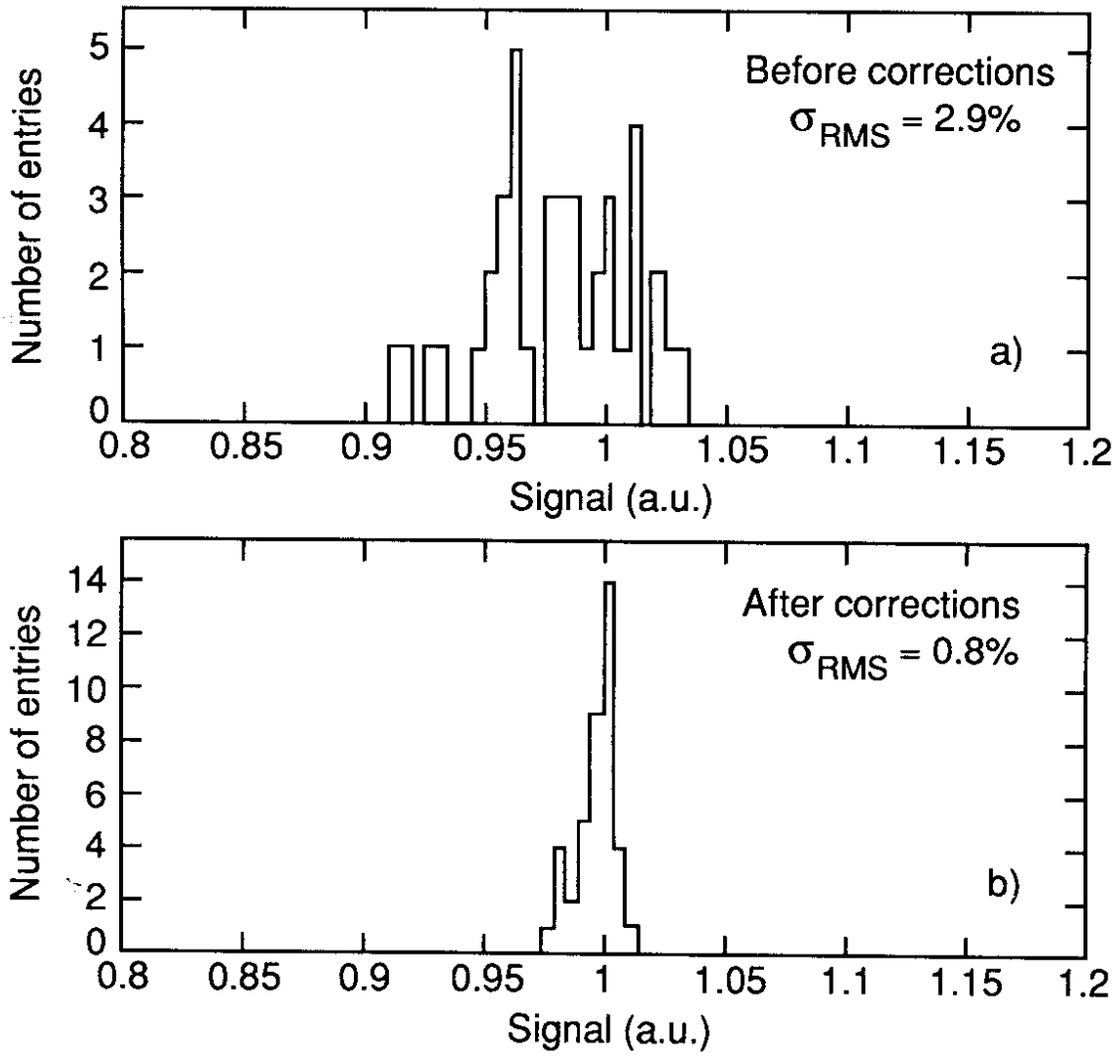
Number of entries
Before corrections
σ_{RMS} = 2.9%
a)
Signal (a.u.)
Number of entries
After corrections
σ_{RMS} = 0.8%
b)
Signal (a.u.)

Fig. 7

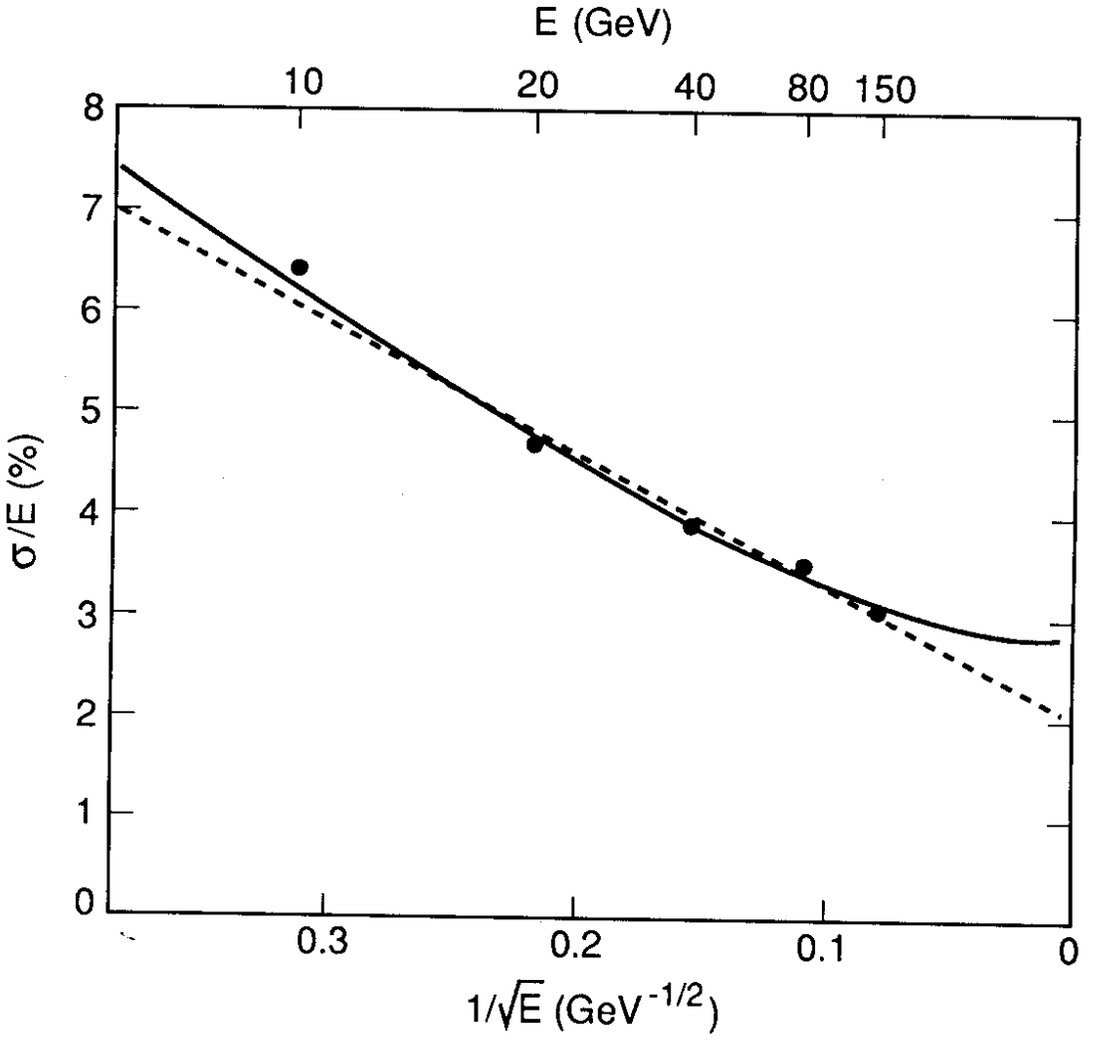

Fig. 8

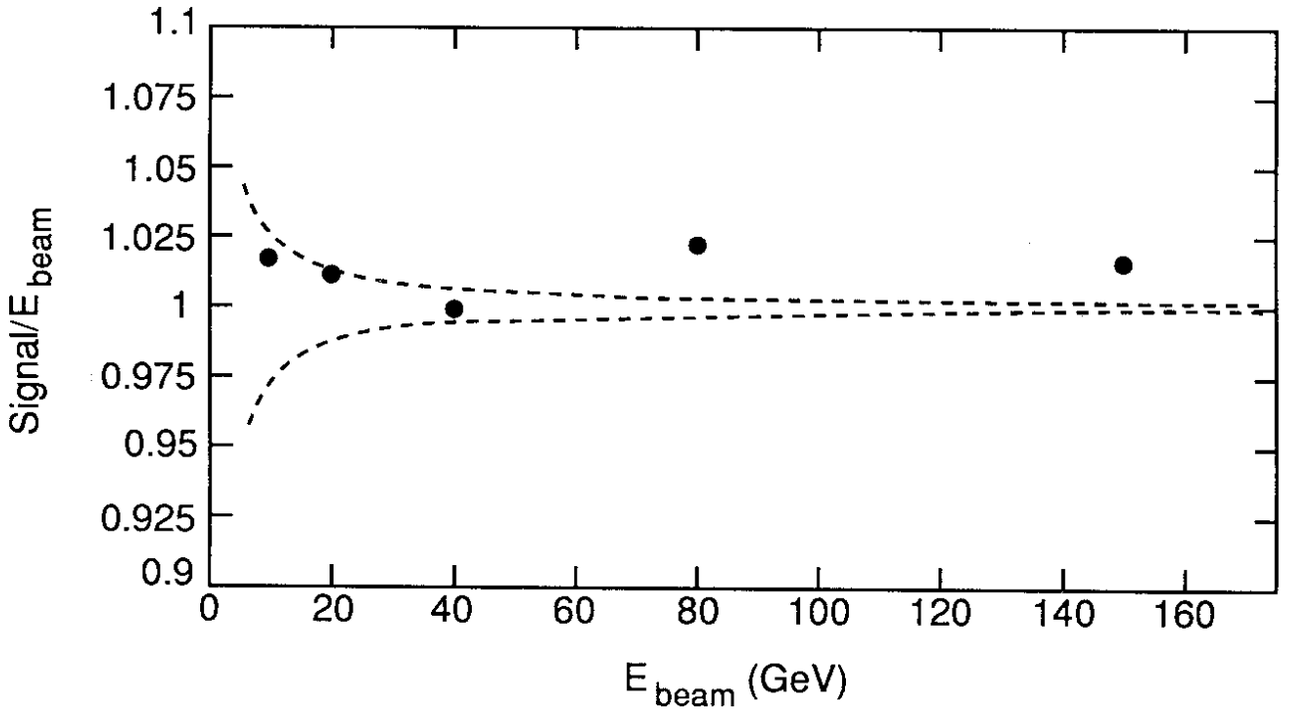
1.1
1.075
1.05
1.025
1
0.975
0.95
0.925
0.9
Signal/E beam
0
20
40
60
80
100
120
140
160
E beam (GeV)

Fig. 9

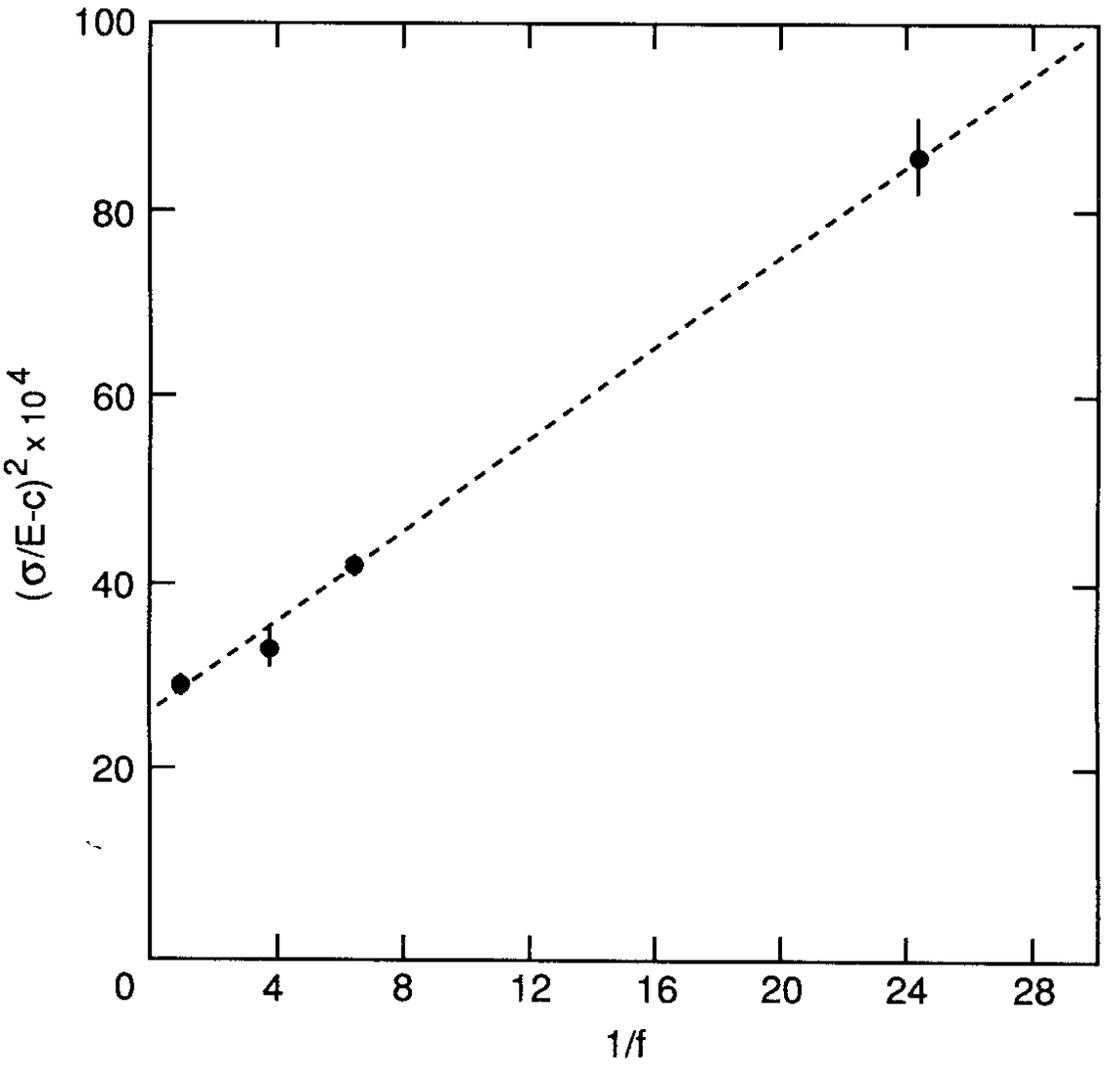

Fig. 10

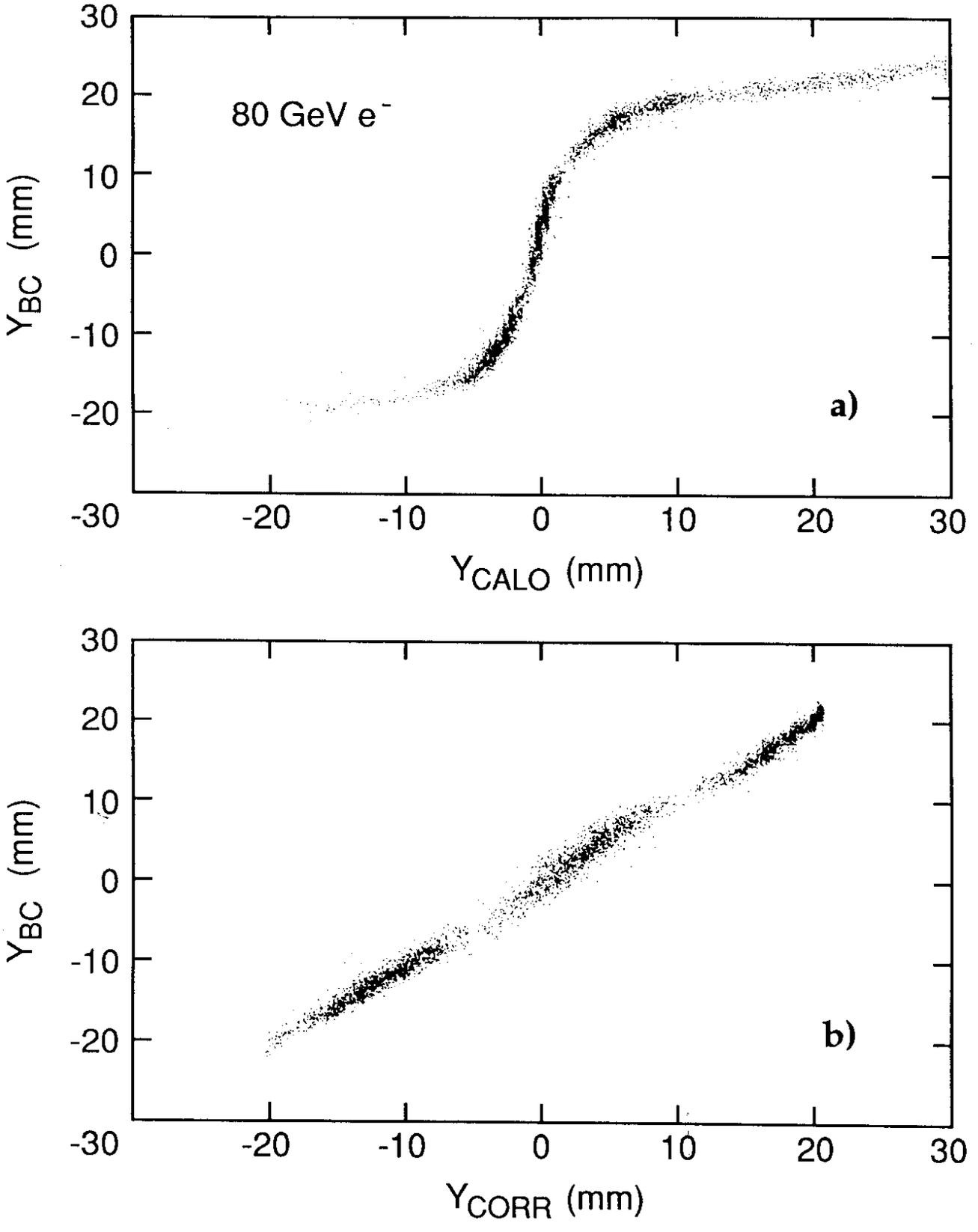

Fig. 11

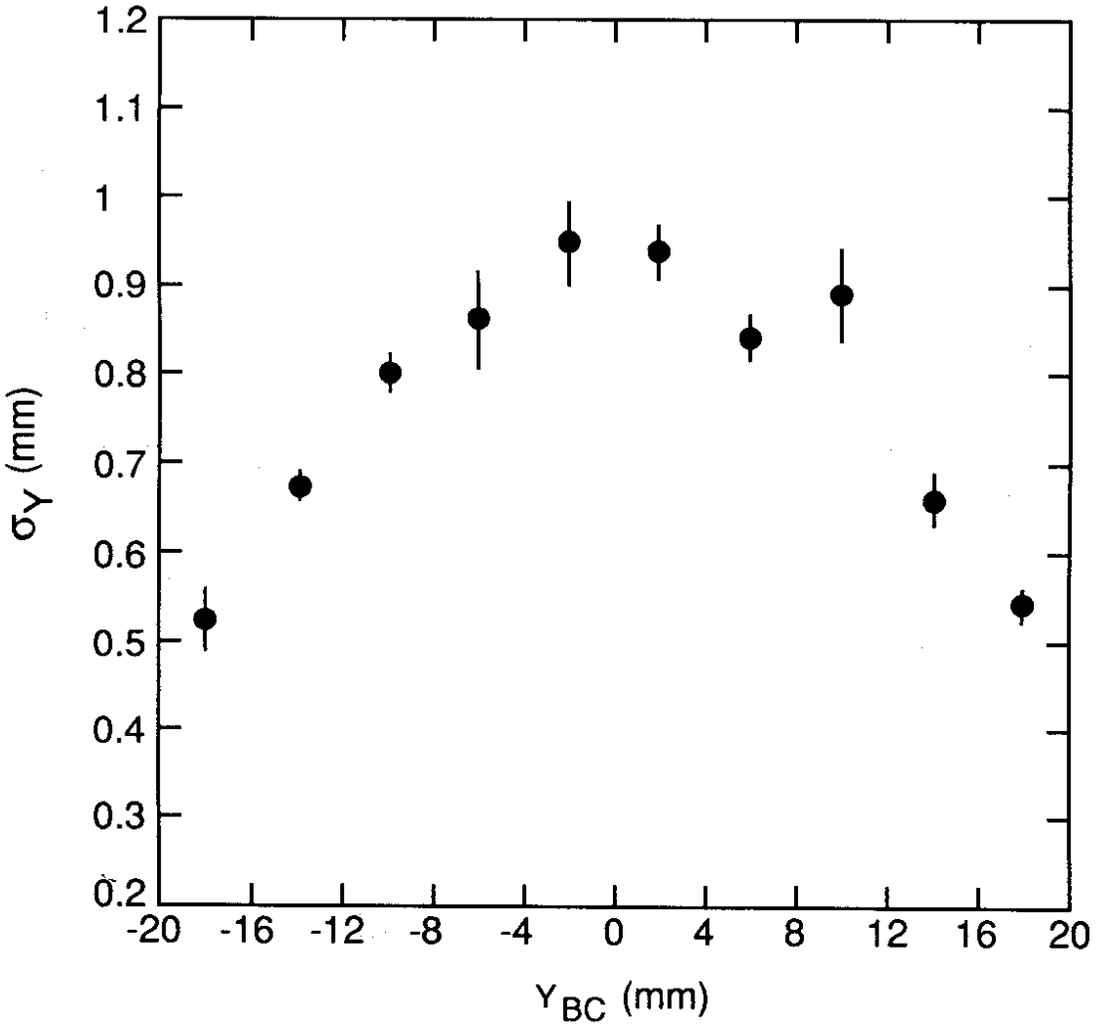
1.2
1.1
1
0.9
0.8
0.7
0.6
0.5
0.4
0.3
0.2
σ_Y (mm)
-20
-16
-12
-8
-4
0
4
8
12
16
20
Y_{BC} (mm)

Fig. 12

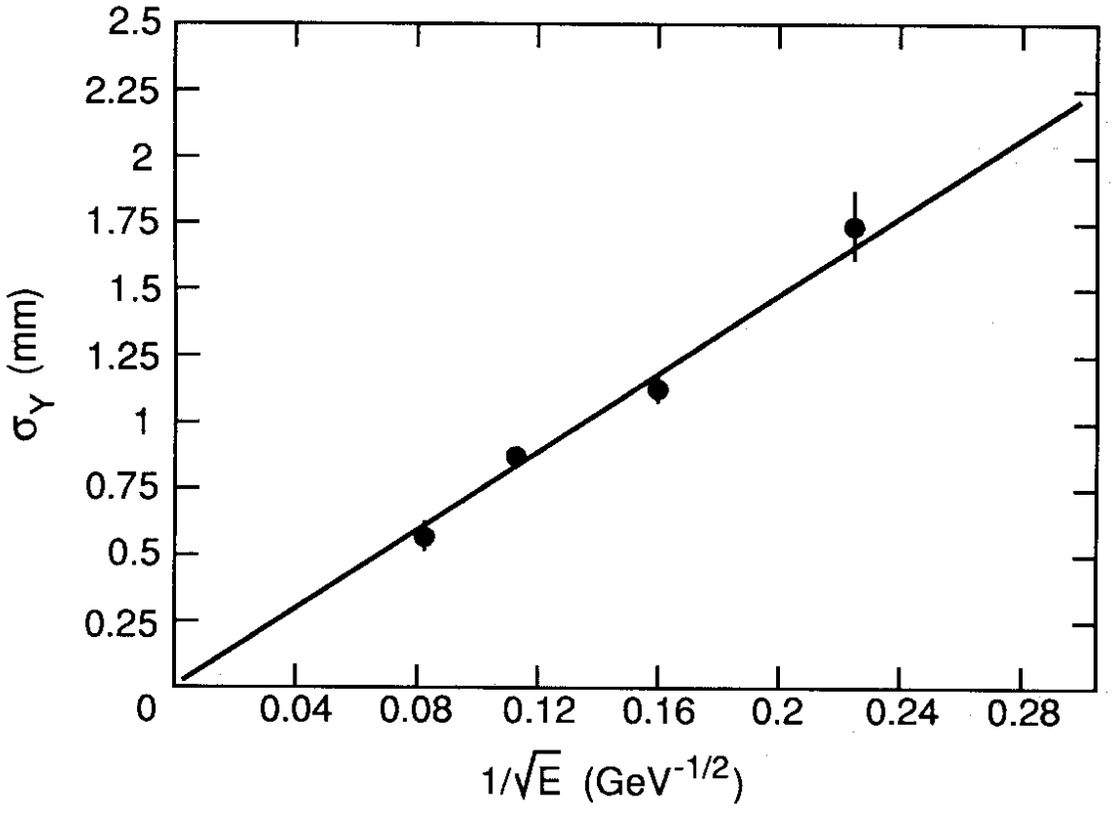
2.5
2.25
2
1.75
1.5
1.25
1
0.75
0.5
0.25
0
σ_Y (mm)
0.04
0.08
0.12
0.16
0.2
0.24
0.28
$1/\sqrt{E}$ ($GeV^{-1/2}$)

Fig. 13

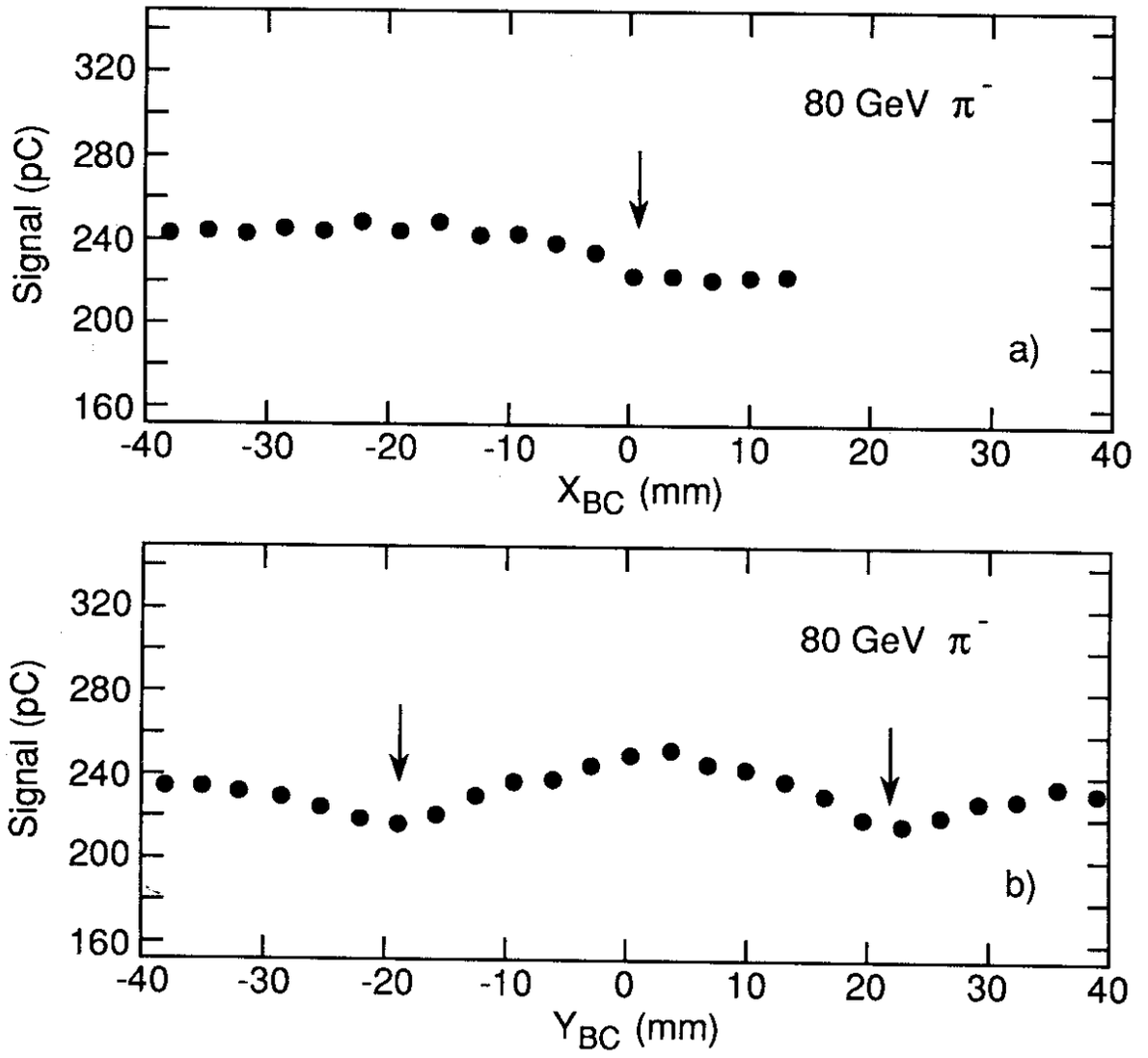
80 GeV π⁻
a)
Signal (pC)
320
280
240
200
160
-40
-30
-20
-10
0
10
20
30
40
X_BC (mm)
80 GeV π⁻
b)
Signal (pC)
320
280
240
200
160
-40
-30
-20
-10
0
10
20
30
40
Y_BC (mm)

Fig. 14

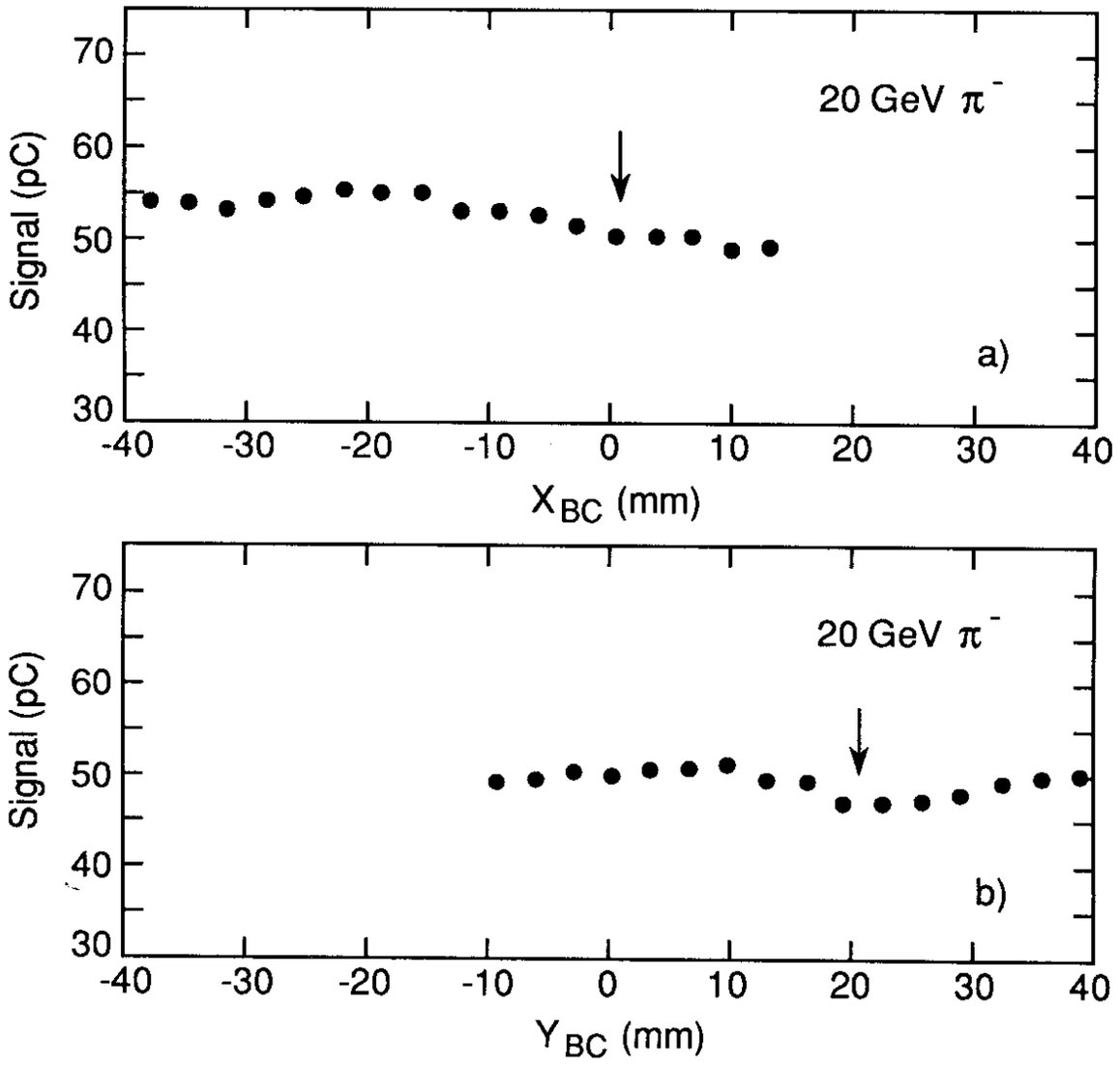
70
60
50
40
30
Signal (pC)
20 GeV π⁻
a)
-40
-30
-20
-10
0
10
20
30
40
X_BC (mm)
70
60
50
40
30
Signal (pC)
20 GeV π⁻
b)
-40
-30
-20
-10
0
10
20
30
40
Y_BC (mm)

Fig. 15

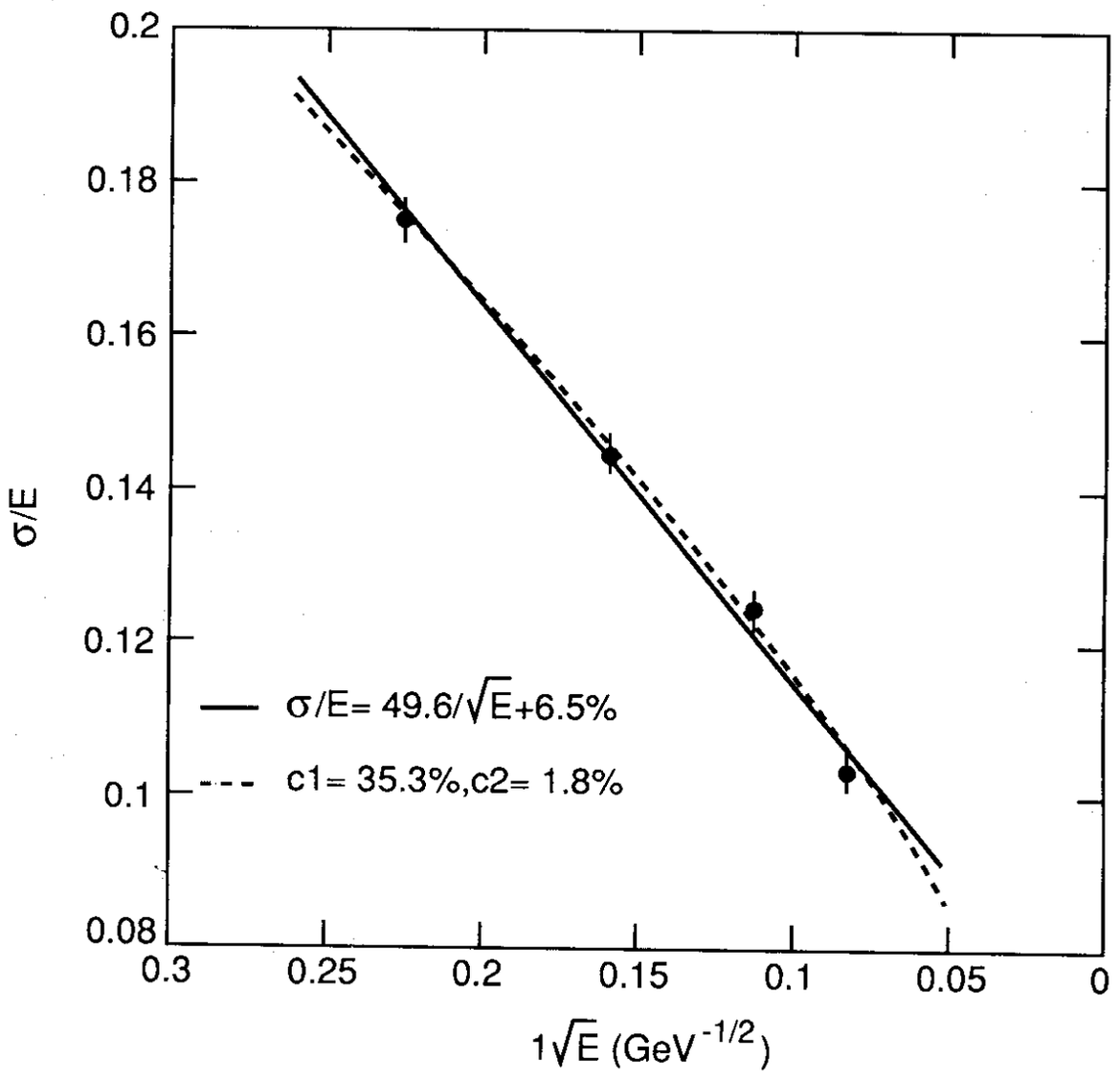
0.2
0.18
0.16
0.14
0.12
0.1
0.08
σ/E
σ/E= 49.6/√E+6.5%
c1= 35.3%,c2= 1.8%
0.3
0.25
0.2
0.15
0.1
0.05
0
1√E (GeV^-1/2)

Fig. 16

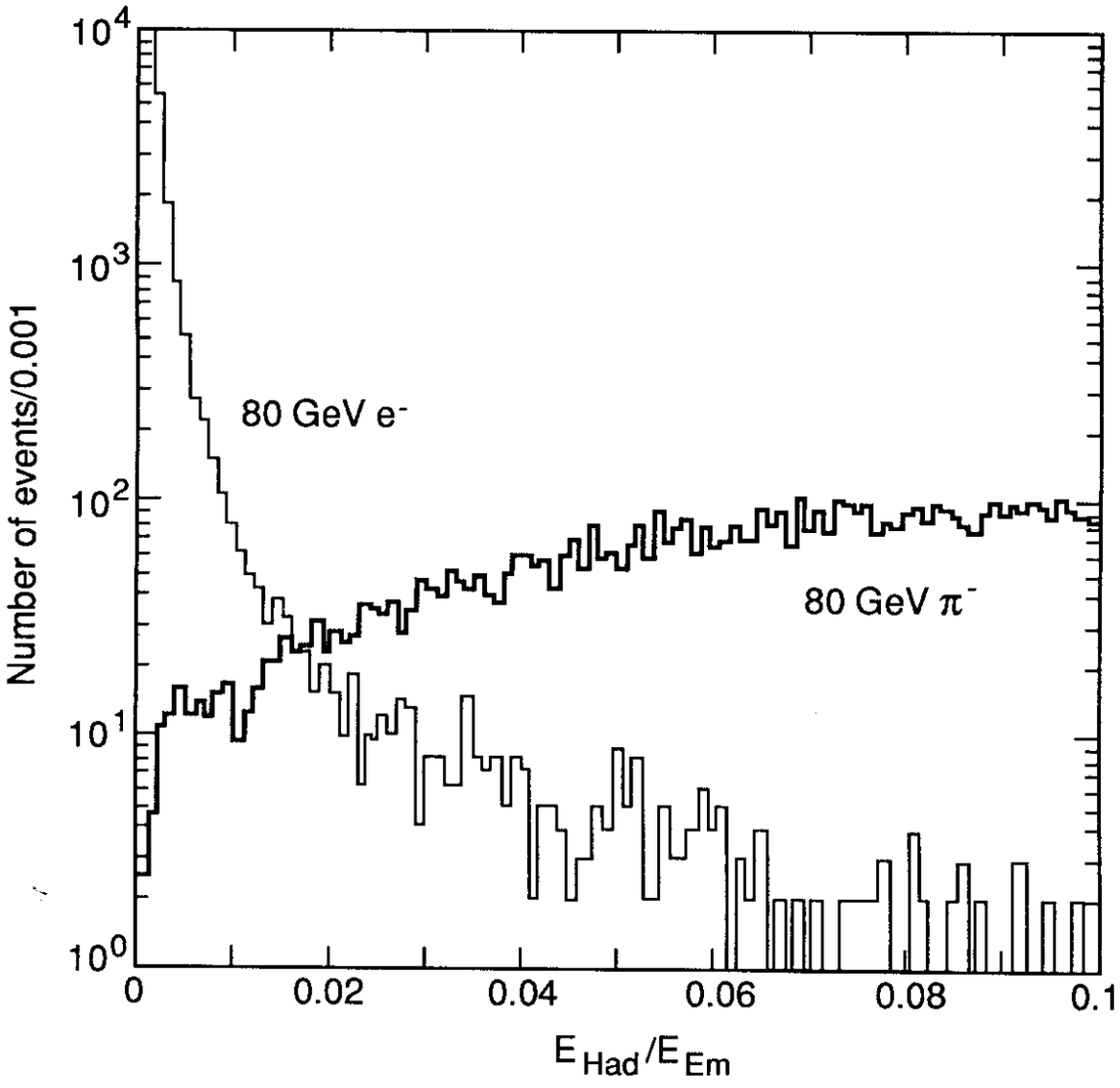
Number of events/0.001
10^4
10^3
10^2
10^1
10^0
80 GeV e^-
80 GeV π^-
0
0.02
0.04
0.06
0.08
0.1
E_{Had}/E_{Em}

Fig. 17

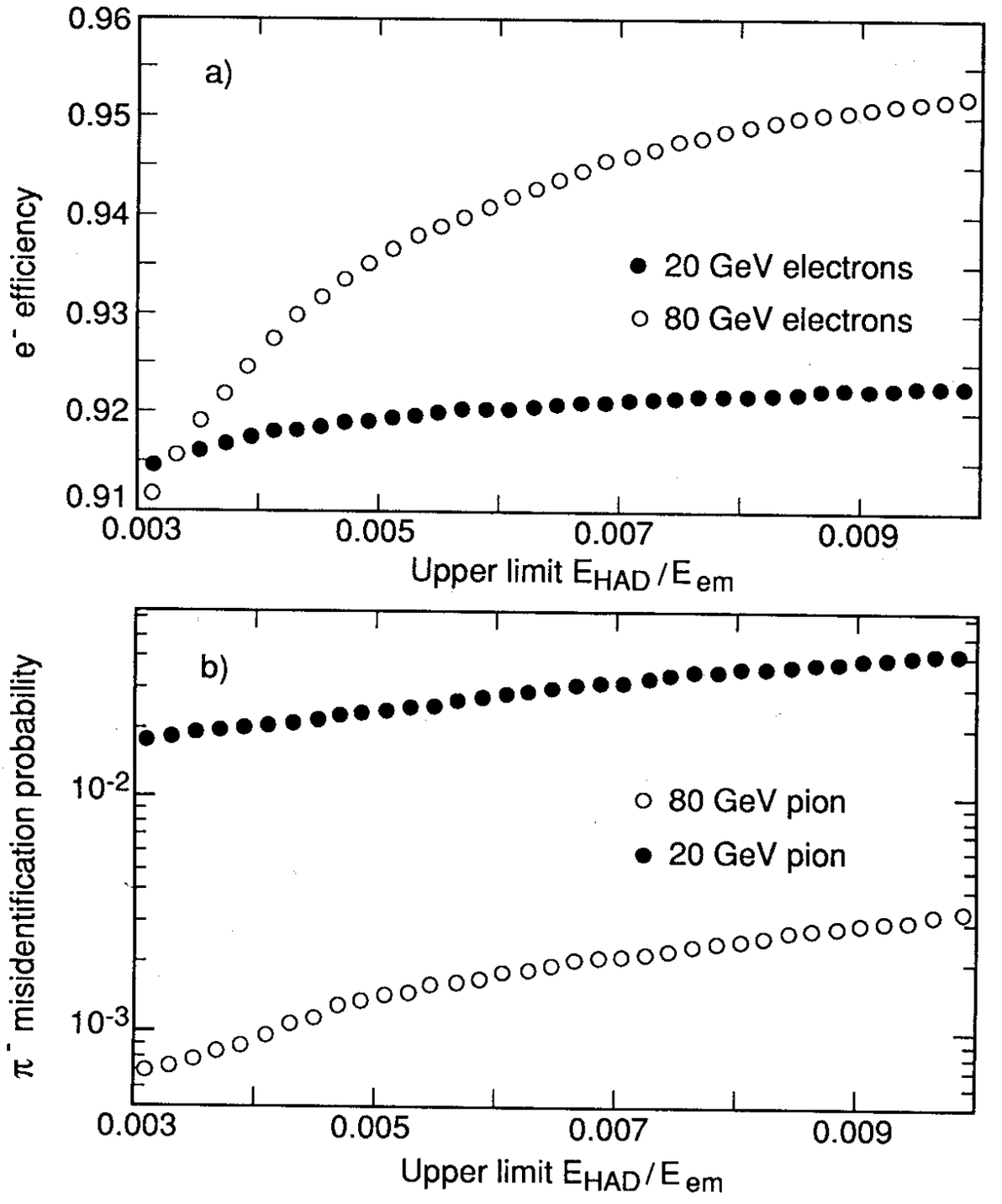
a)
0.96
0.95
0.94
0.93
0.92
0.91
e⁻ efficiency
20 GeV electrons
80 GeV electrons
0.003
0.005
0.007
0.009
Upper limit E_HAD / E_em
b)
10⁻²
10⁻³
π⁻ misidentification probability
80 GeV pion
20 GeV pion
0.003
0.005
0.007
0.009
Upper limit E_HAD / E_em

Fig. 18

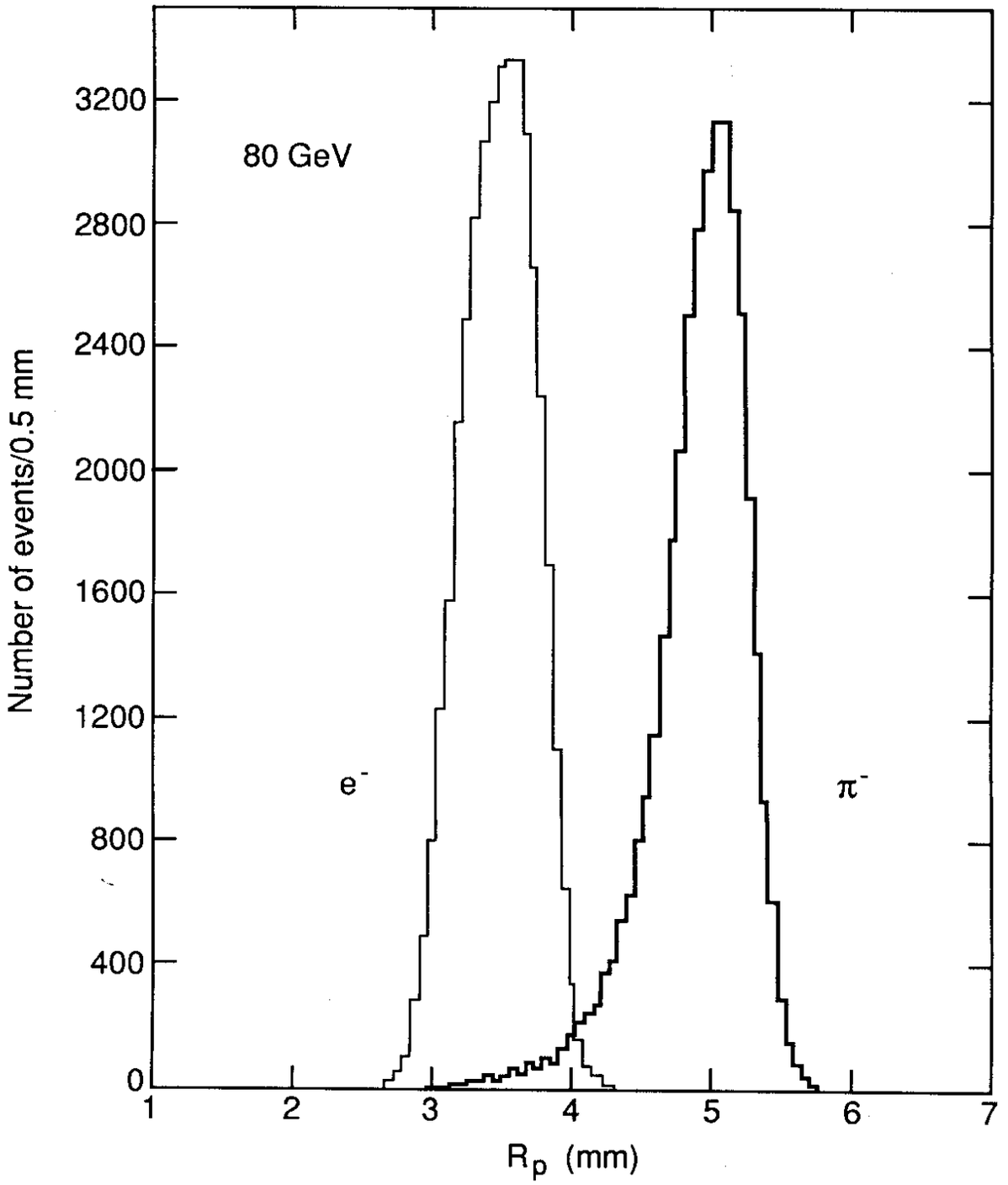
80 GeV
e⁻
π⁻
Number of events/0.5 mm
R_p (mm)
0
400
800
1200
1600
2000
2400
2800
3200
1
2
3
4
5
6
7

Fig. 19

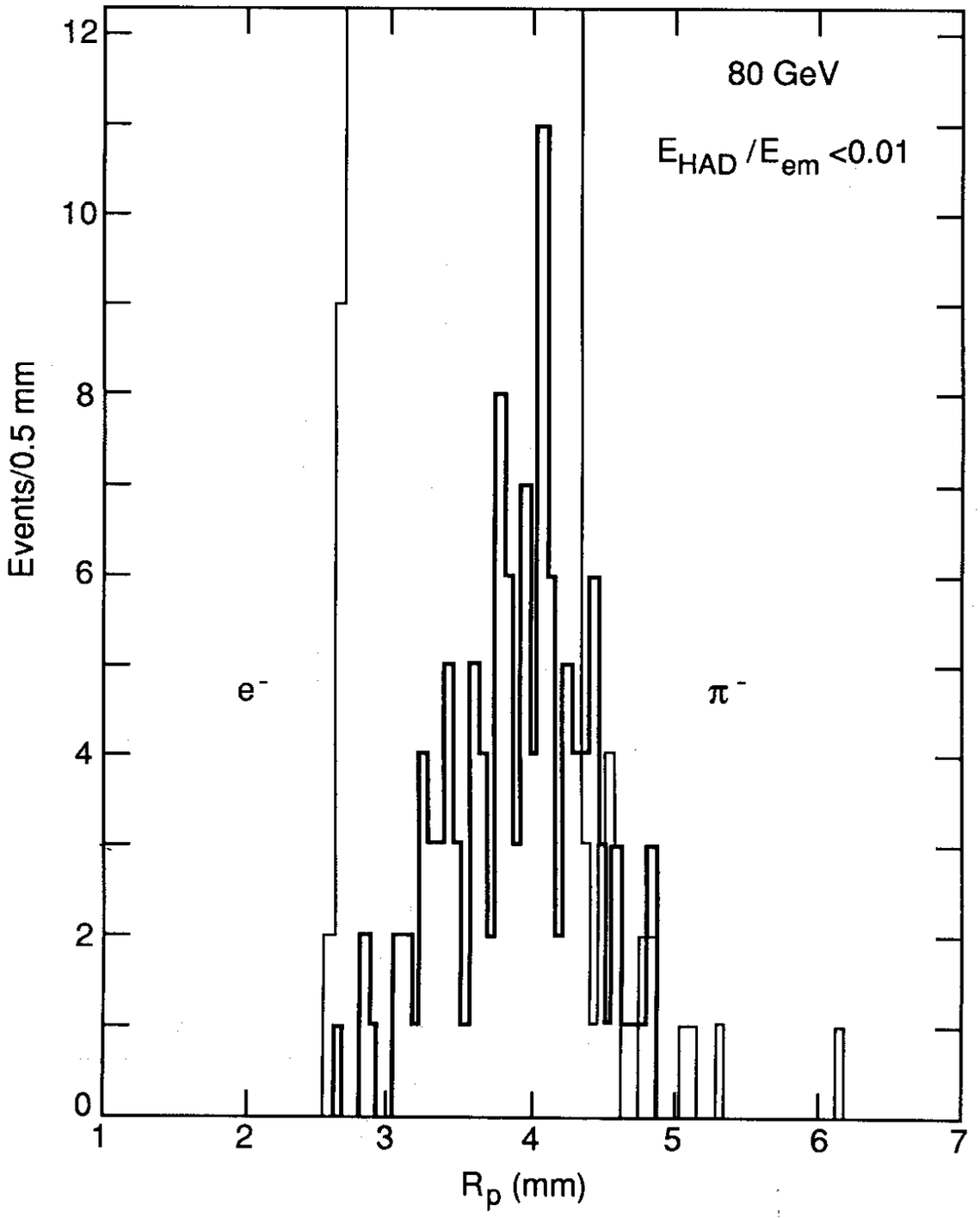

Fig. 20

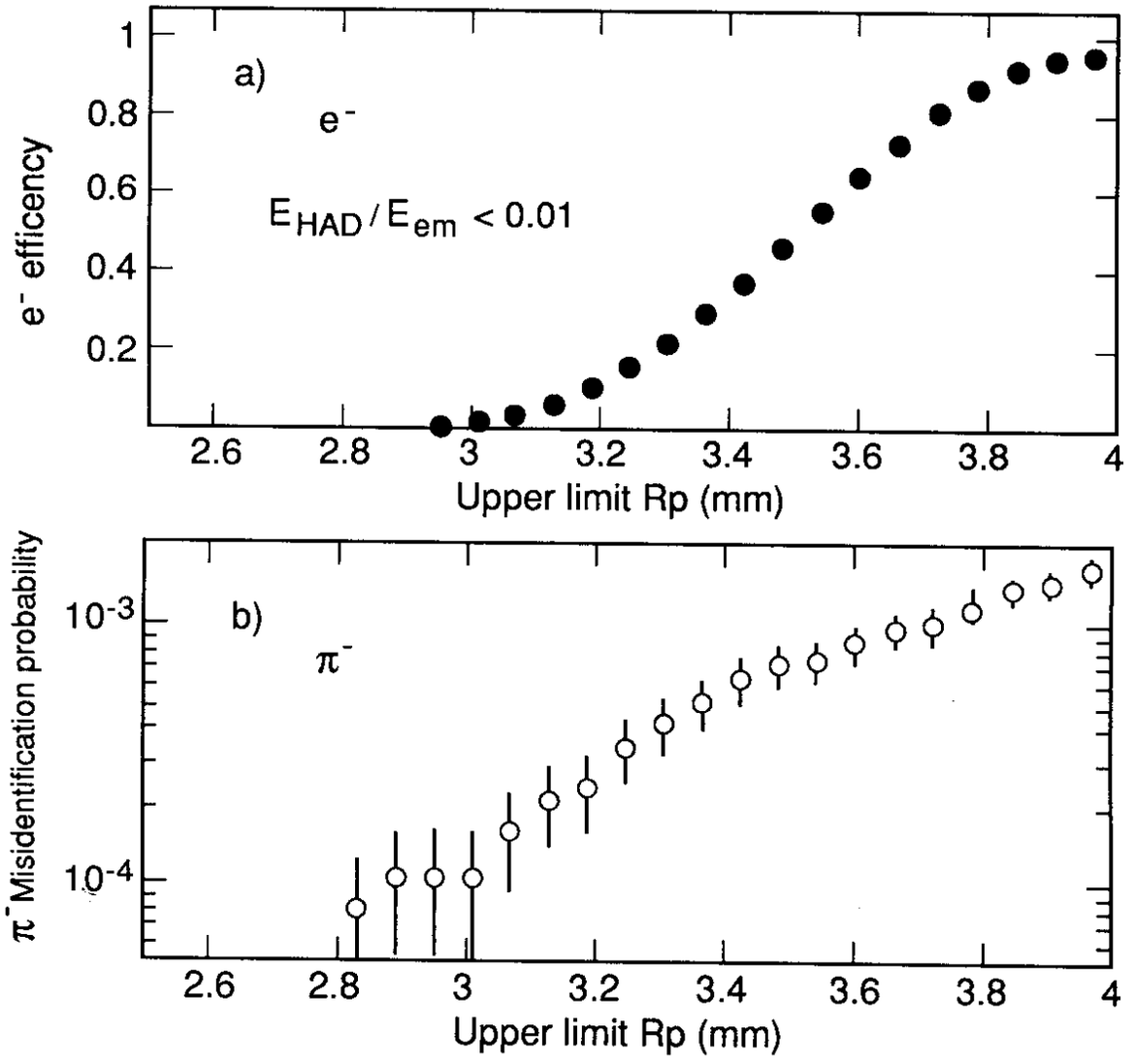
a)
e⁻
E_HAD / E_em < 0.01
e⁻ efficency
1
0.8
0.6
0.4
0.2
2.6
2.8
3
3.2
3.4
3.6
3.8
4
Upper limit Rp (mm)
b)
π⁻
π⁻ Misidentification probability
10⁻³
10⁻⁴
2.6
2.8
3
3.2
3.4
3.6
3.8
4
Upper limit Rp (mm)

Fig. 21

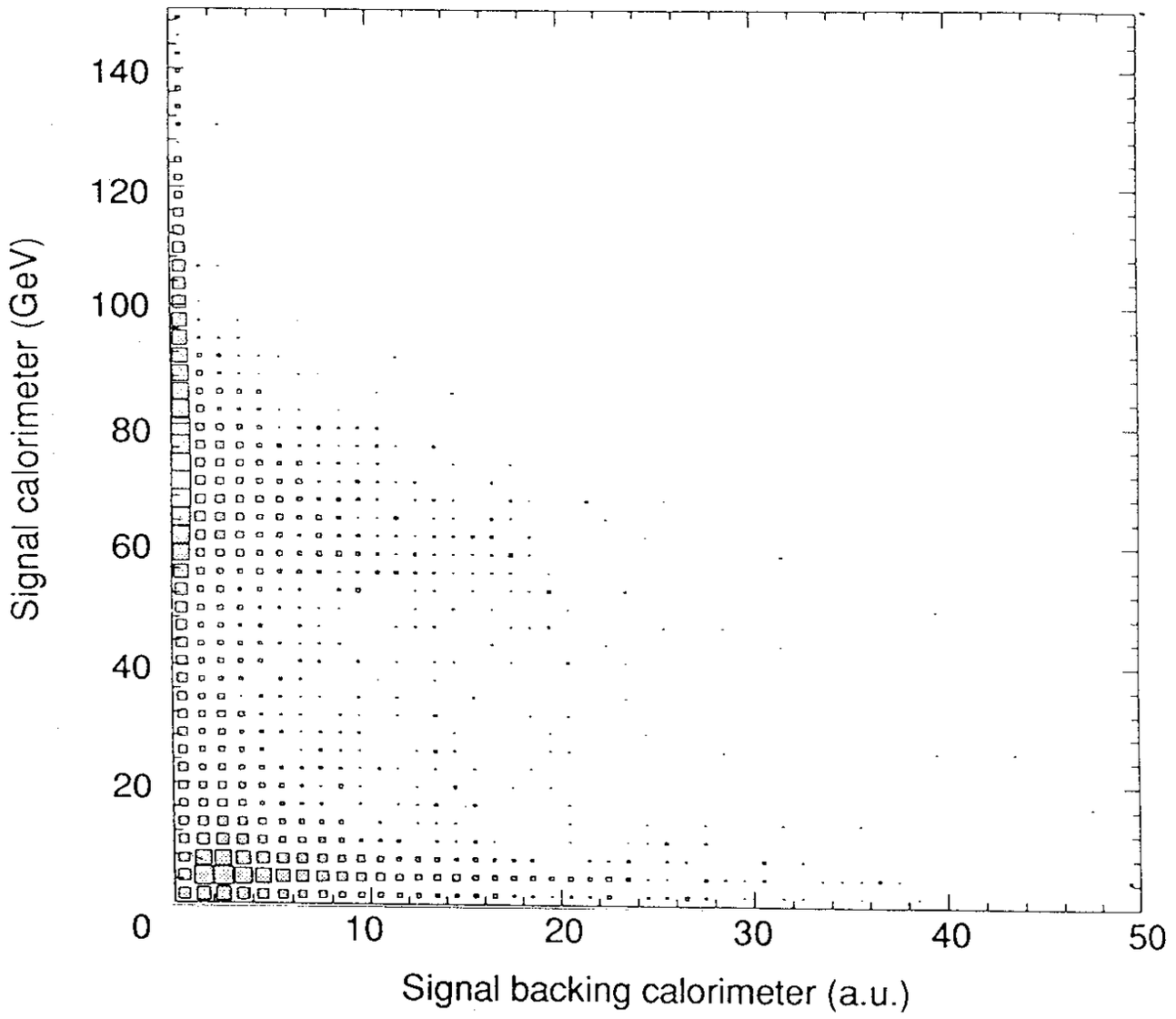
Signal calorimeter (GeV)
140
120
100
80
60
40
20
0
10
20
30
40
50
Signal backing calorimeter (a.u.)

Fig. 22

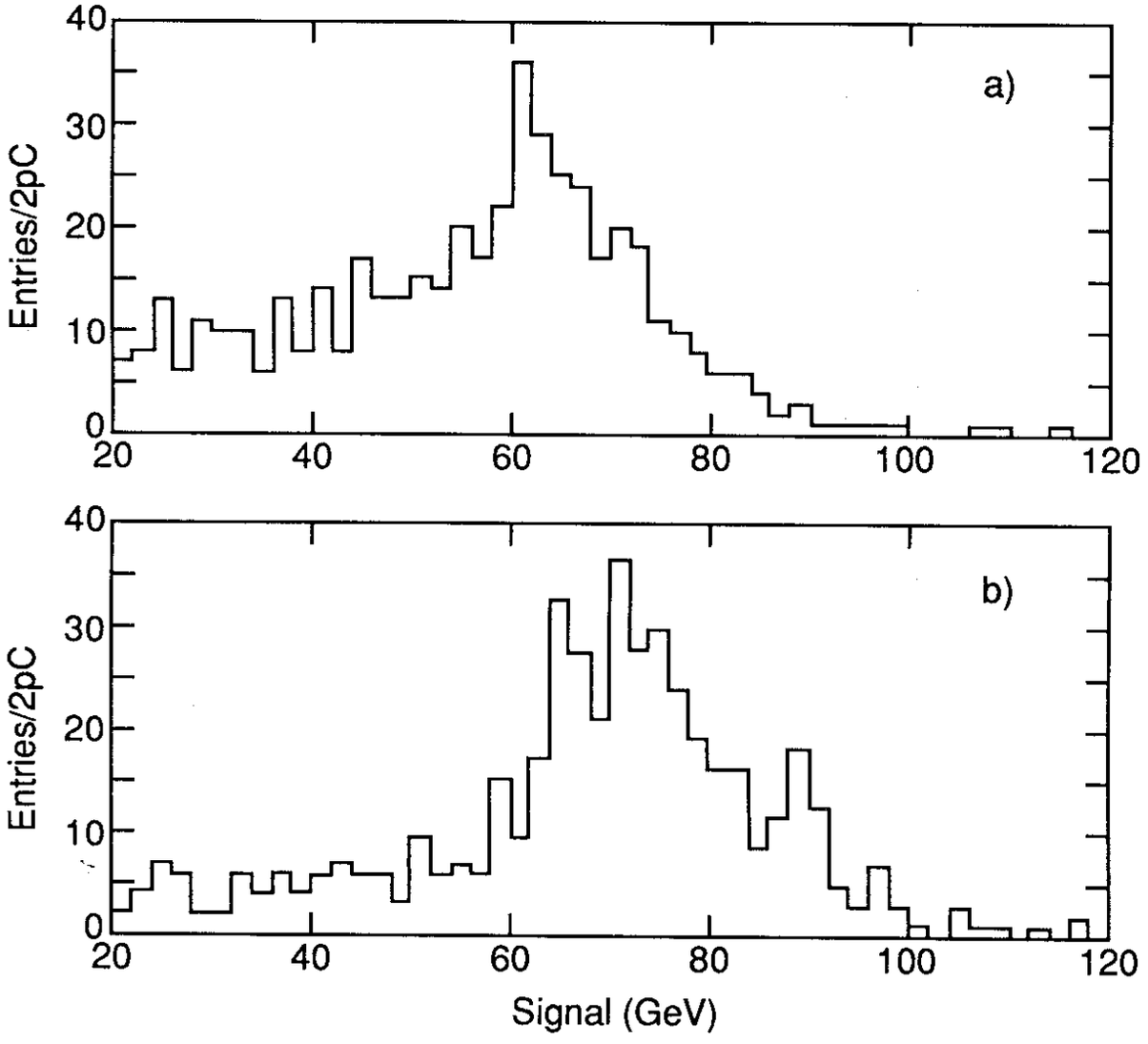
a)
b)
Entries/2pC
Entries/2pC
Signal (GeV)
0
10
20
30
40
20
40
60
80
100
120

Fig. 23

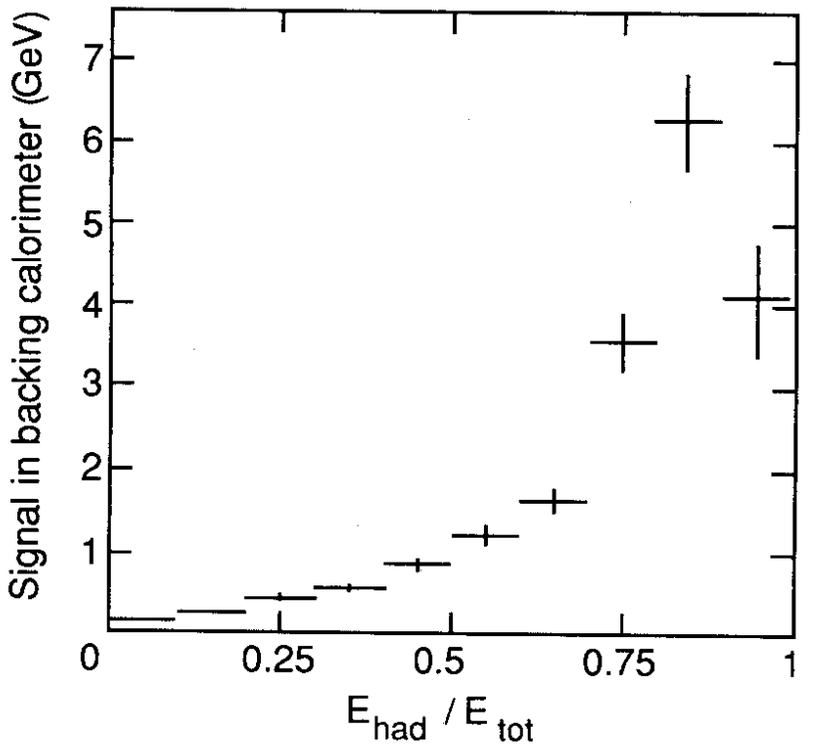
Signal in backing calorimeter (GeV)
7
6
5
4
3
2
1
0
0.25
0.5
0.75
1
E had / E tot

Fig. 24

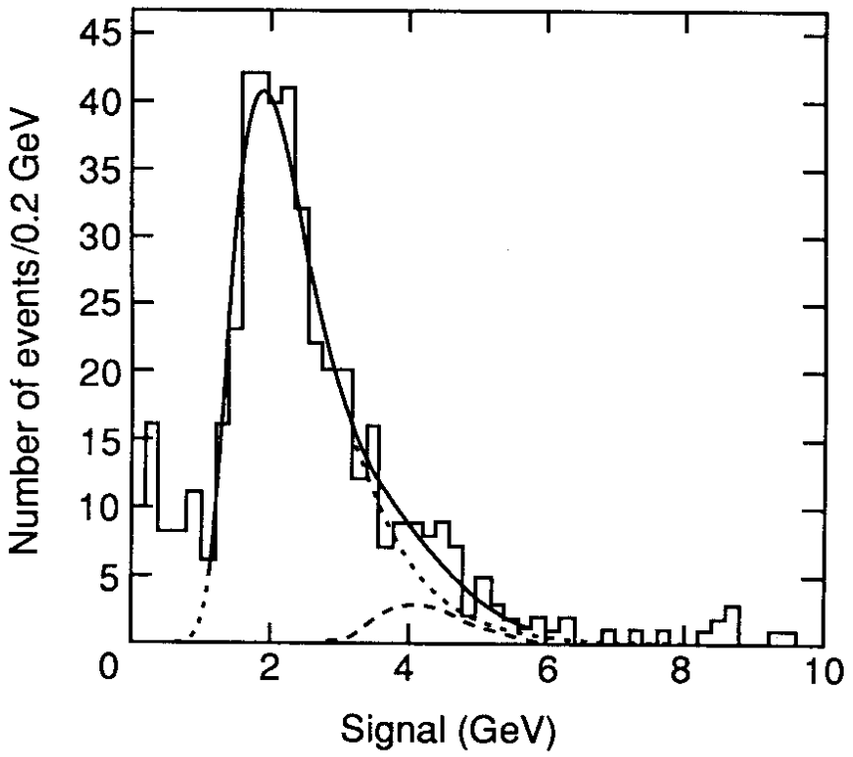
Number of events/0.2 GeV
Signal (GeV)
0
5
10
15
20
25
30
35
40
45
2
4
6
8
10

Fig. 25